
Bachelor Thesis

# Improved parametrisation of target heat flux in W7-X

Johannes Droste

Reviewers:
Prof. Dr. Ralf Schneider
Prof. Dr. Thomas Klinger

Institute of Physics
University of Greifswald
Januar 15, 2024

# Contents

# 1 Abstract

In this work an approach to parametrise the complex structure of the heat-flux distribution on the targets of the Wendelstein 7-X (W7-X) target load pattern is presented. A tool is introduced that allows to fit and parametrise the heat-flux distribution onto the divertor target. The analysis shows that the strike line exhibits multiple features along the target that are sometimes overlapping. This is particularly pronounced in high density conditions. The developed tool allows for the separation and characterisation of these features. The clear identification of the different features and their change with plasma conditions and the comparison to connection length maps suggest the existence of several separate heat transport channels. In addition, the methodology allows the localization of regions that show material deposition, mis-alignment or target surface damage. All these effects will invalidate the present heat-flux calculations. Fitting the main strike line heat-flux footprint allows to extract key parameters, such as heat-flux channel width and heat-flux maximum, for investigating the heat exhaust behavior. Previous analysis was insufficient for the characterization of the heat load patterns as it was not able to account for the rich structure that was observed. The influence of time dependent parameters like toroidal plasma current and its influence on strike line position is also investigated.

# 2 Introduction

Nuclear fusion, which has been researched since the early 1950's, is and has been for some time a promising path to unlimited clean energy. Among various experimental approaches to achieve controlled nuclear fusion, the furthest developed types of fusion devices use magnetic fields produced by superconducting coils to confine a plasma [1]. On this path to a nuclear fusion power plant, two different concepts, the Tokamak and Stellarator, are being pursued [2]. The latter offers several advantages in the pursuit of controlled nuclear fusion. Unlike Tokamaks, they have the inherent capability to sustain a steady-state plasma. The Max-Plank Institute for Plasma physics (IPP) operates the worlds largest stellarator fusion device Wendelstein 7-X in Greifswald, Germany.

Understanding and predicting the heat transport in the region outside the confined plasma, called the scrape of layer (SOL), is of significant interest in order to design a fusion power plant that can handle the heat loads on the first wall. In W7-X a so called island divertor is deployed to efficiently extract heat and fusion products from the reactor chamber. The target modules of the island divertor intersect the flux surfaces of magnetic islands, which form outside the confined plasma. The targets in W7-X are made from carbon, which limits the amount of heat-flux they can withstand to around $10\,\frac{\mathrm{MW}}{\mathrm{m}^2}$ [3]. Using IR thermography, the heat-flux onto the targets is measured, providing data for analyzing the spatial and temporal distribution of heat loads, essential for the assessment and optimization of plasma performance and material integrity in the reactor. A promising model to predict the target heat-flux is the Simple Model for Loads in Island Divertor (SMoLID) by Amit Kharwandikar. It depends however on accurate target heat-flux measurements to determine scaling factors.

This thesis delves into an approach introduced by Dr. David Bold in [4] for parametrising the complex structure of the heat-flux distribution of the W7-X targets. A tool computational is presented that allows the fitting and parametrisation of the heat flux distribution on the divertor target. The observed strike line profile differs significantly from its expected shape in some cases. Particularly in higher-density conditions, multiple features along the target in the toroidal direction are pronounced, requiring investigation to find their origin. A thorough study into deposits on the target surface as source of these additional features is done. Transport mechanisms in the SOL, parallel and perpendicular transport as well as Drifts, are discussed. An attempt is made to connect the strike line behavior with transport mechanisms, which has proven difficult, based on only target heat-flux data. Finally, the findings are summarized and suggestions to further improve the fitting routine are are given.

# 3 Nuclear Fusion

## 3.1 Fusion Reactions

For fusion to occur, the nuclei must overcome the coulomb barrier to come within the distances required. The two nuclei need to come close enough for long enough so that the strong attractive nuclear force can take over and overcome the repulsive electrostatic force. Quantum effects, such as tunneling through the Coulomb barrier, allow the fusion reactions to occur at lower energy than one would expect from classical theory. The reaction rate of fusion is $R = n_1 n_2 \langle \sigma \nu \rangle$, where $\sigma$ is the reaction cross-section and $\nu$ is the relative velocity. It determines in large part the viability of fusion fuels. As can be seen in fig. 1, of the four shown reactions

$$\begin{aligned} \mathrm{D}^2 + \mathrm{T}^3 &\rightarrow \mathrm{He}^4 + \mathrm{n}^1 + 17.6\,\mathrm{MeV} \\ \mathrm{D}^2 + \mathrm{D}^2 &\rightarrow \mathrm{He}^3 + \mathrm{n}^1 + 3.27\,\mathrm{MeV} \\ \mathrm{D}^2 + \mathrm{D}^2 &\rightarrow \mathrm{T}^3 + \mathrm{H}^1 + 4.03\,\mathrm{MeV} \\ \mathrm{D}^2 + \mathrm{He}^3 &\rightarrow \mathrm{He}^4 + \mathrm{H}^1 + 18.3\,\mathrm{MeV} \end{aligned} \tag{1}$$

the reactivity $\langle \sigma \nu \rangle$ of Deuterium (D) and Tritium (T) at 30 keV is about two orders of magnitude larger than for the next best fusion fuel of pure deuterium (D-D). The energy produced per reaction is also one of the highest of any fusion fuel. This is why D-T fusion is preferred fuel for use in power plants. Deuterium is stable and present in sufficient quantities in water. Tritium is radioactive with a half-life of about 12.6 years. It can however be bred using a blanket surrounding the reactor which contains lithium. The neutrons released in the fusion reaction (eq. 1) are slowed and absorbed by this blanked, generating the tritium needed (eq. 2). In addition, 4/5 of the energy generated is carried by the neutron, which is being absorbed volumetrically by the blanket, making power exhaust much easier [1]. Neutron multipliers like Beryllium are required to get to a breeding ratio above one to make up for neutrons not absorbed by Lithium.

$$\begin{aligned} \mathrm{Li}^6 + \mathrm{n}^1 &\rightarrow \mathrm{He}^4 + \mathrm{T}^3 + 4.80\,\mathrm{MeV} \\ \mathrm{Li}^7 + \mathrm{n}^1 &\rightarrow \mathrm{He}^4 + \mathrm{T}^3 + \mathrm{n}^1 - 2.46\,\mathrm{MeV} \end{aligned} \tag{2}$$

Although initial heating has to be provided for the plasma to reach fusion conditions, $\alpha$-particles generated by the fusion process are envisioned to provide the main heating in a burning plasma. For D-T, the $\mathrm{He}^4$ carries 20 % of the fusion energy. If adequate confinement conditions are achieved, the so called ignition point is reached, at which the fusion reaction increases the plasma temperature without external heating (fig. 2). The ignition condition defines the parameters a fusion power plant should reach. It is characterized by the Lawson criterion and depends on the ion density $n_i$, temperature $T_i$ and the energy confinement time $\tau_E$ [6]

$$n_\mathrm{e} T_\mathrm{e} \tau_E \geq 5 \cdot 10^{21} \frac{\mathrm{keV} \cdot \mathrm{s}}{\mathrm{m}^3}. \tag{3}$$

## 3.2 Magnetic confinement

Magnetic confinement fusion is the most promising and furthest developed path to fusion. To achieve fusion using this approach, a plasma with the thermal energy above 30 keV must be held with a magnetic field [2]. To confine the plasma inside a reactor and

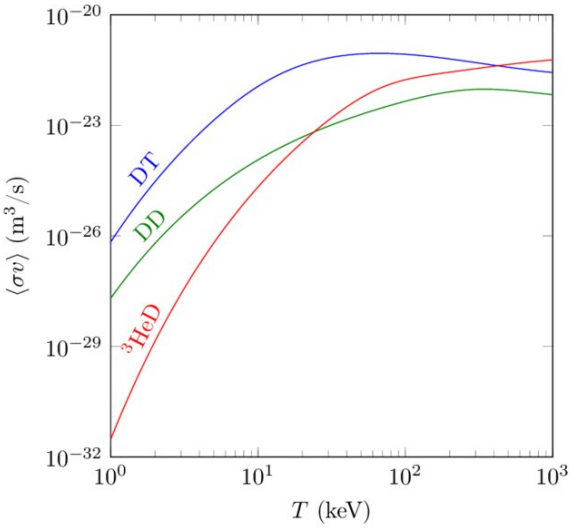


**Figure 1:** Reactivity $\langle \sigma \nu \rangle$ for D-T, D-D and D-He$^3$ fusion reactions in m$^3$s$^{-1}$ for different plasma temperatures [5].

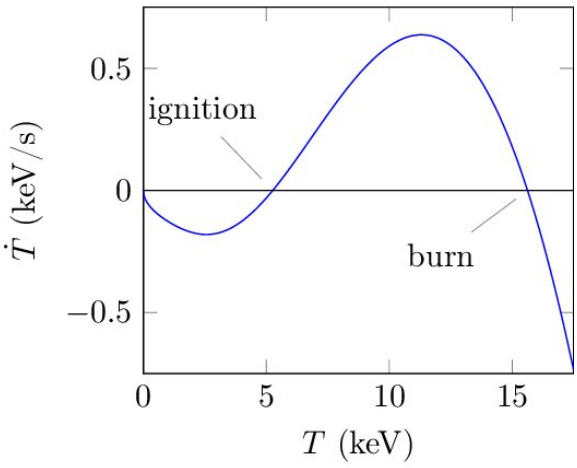


**Figure 2:** The $\alpha$-heating rate $\dot{T}$ plotted against a hypothetical fusion reactor. After ignition the temperature increases without external heating until a stable equilibrium is reached, reproduced from [5].

provide a sufficiently large $\tau_E$ (see 3) with $\tau_E = W_{\text{plasma}}/P_{\text{heat}}$, magnetic fields produced by superconducting coils are used. In a uniform magnetic field the charged particles follow a cyclotron gyration around the magnetic field lines. To achieve confinement, the field lines are bend into a toroidal shape (fig. 4). Since the field lines are closer together towards the center of the toroid, the ions and electrons experience a change in the magnetic field **B**. This induces a drift where the direction depends on the charge of the particle $q$, leading to a charge separation:

$$v_{\nabla B} = \frac{W_\perp \times \nabla \mathbf{B}}{q \cdot B^3}, \tag{4}$$

where **B** is the magnetic field and $W \perp$ is the perpendicular kinetic energy of the particle. The charge separation establishes an electric field **E**. This induces a drift independent of the charge horizontally outwards [2, 6]

$$v_{\mathbf{E}\times\mathbf{B}} = \frac{\mathbf{E} \times \mathbf{B}}{B^2}. \tag{5}$$

To combat this, a rotational transform of the toroidal magnetic field is introduced. This allows the electrons to move freely along magnetic field lines to cancel out the vertical potential differences via parallel return currents. As found by [8, 9] and laid out by [10], there are three ways to achieve the required helical field component.

In tokamaks, an electric current is induced in the plasma via a central Transformer coil. In stellarators like W7-X, the magnetic axis is made non-planar so that the torsion of **B** is non zero. Additionally, the flux surfaces are elongated in such a

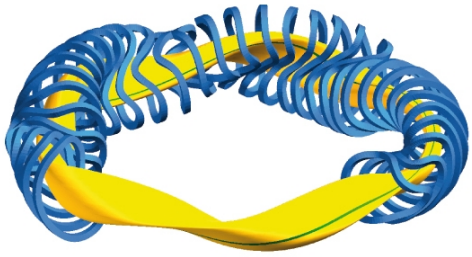

**Figure 3:** Magnetic coils and Plasma of W7-X. A single magnetic field line is shown in green [7].

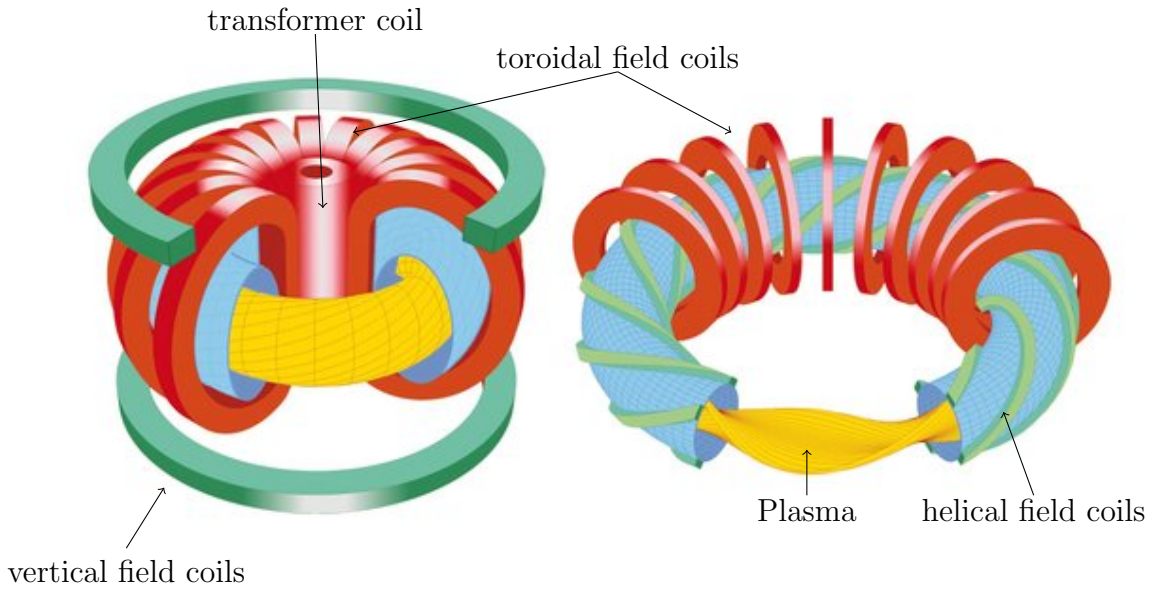


**Figure 4:** Example configuration of tokamak (left) and stellarator coils (right) [11].

way that they rotate poloidally. As can be seen in fig. 4, an additional set of coils helically wound around the torus is added. Because of Ampère's circuital law $\sum \mathbf{B}_{\mathrm{pol}} = \mu_0 I$ the sum of the poloidal magnetic field $B_{\mathrm{pol}}$ must be zero in a stellarator, since there is no induced toroidal current in the plasma. This is why the helical field coils carry opposing currents, generating opposing poloidal magnetic fields. In W7-X, the helical field coils have been integrated into the toroidal field coils as can be seen in fig. 3 [12].

Collisions between trapped particles and passing particles generate a bootstrap current in the presence of a pressure gradient:

$$j_{\mathrm{b}} \sim -\varepsilon^{1/2} \frac{1}{B_{\mathrm{pol}}} \frac{\mathrm{d}p}{\mathrm{d}r} \tag{6}$$

where $\varepsilon$ is the inverse aspect ratio. This toroidal current induces a poloidal magnetic field. The bootstrap current in W7-X is much smaller than in similar sized tokamaks, due to the optimisation.

## 3.3 Divertor Concept

Even though 80 % of the fusion energy is leaving the reactor volume via neutrons, 20 % will have to be extracted from the plasma. Therefore, any reactor needs to be able to avoid excessive heat loads interacting with the inner reactor wall. W-7X uses a so called island divertor. As its name suggests, it exploits the existence of large magnetic islands outside the main confined plasma. These islands originate from small radial field perturbations $b_{mn} = B^{\mathrm{r}}_{mn}/B_{\mathrm{tor}}$. A side band Fourier harmonic $B^{\mathrm{r}}_{mn}$ of the radial $B^{\mathrm{r}}$ spectrum tears the flux surfaces apart so that magnetic islands form. $B^{\mathrm{r}}_{mn}$ is resonant to the rotational transform $\iota/2\pi = \imath = M \cdot \frac{m}{n}$, which is the number of poloidal transits $m$ per toroidal transit $n$ of a field line on a toroidal flux surface. $M$ is the number of toroidal field periods, which is $M = 5$ for W7-X. Where $\imath$ is a real number, a magnetic island can form [14, 15]. By adjusting the rotational transform, the position of the magnetic islands and by extend the strike line can be influenced [16]. In W7-X, multiple

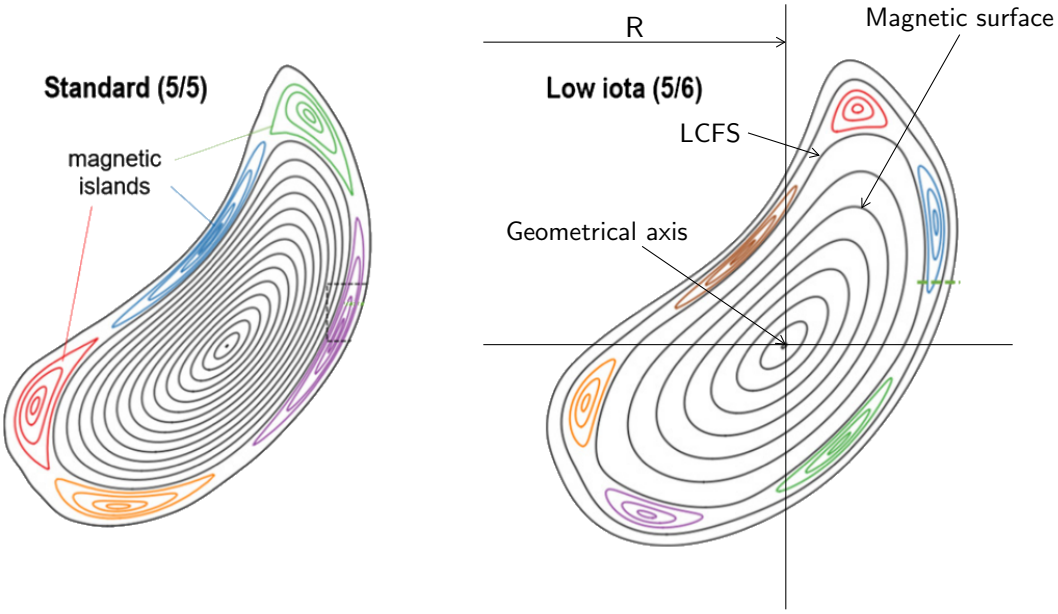


**Figure 5:** Poincaré cross section of the standard (5/5)- and low iota (5/6) magnetic configurations with colored magnetic islands in W7-X [13]. The major radius averaged over one toroidal turn is $R = 5.5\,\mathrm{m}$ for W7-X which is roughly 5 times that of the average minor radius $r$.

island divertor configurations are possible, depending on the chosen rotational transform $\iota$, see fig. 5. Three main configurations are possible, the low, standard and high iota configurations with respective resonances of $\iota = 5/6, 5/5$ and $5/4$ [17]. W7-X is made up of 5 identical segments, called modules. Each module is stellarator symmetric and the device can be effectively described by a single half-module. Each module has an upper and a lower divertor for a total of 10 divertors. The divertor targets are labeled as 1-5u (upper) and 1-5l (lower), see fig. 6. Each of the 10 divertors consists of two poloidally separated parts, a horizontal and a vertical target. Between them is a gap for trapping the neutral particles for pumping. The horizontal divertor consists of two toroidally separated targets with a middle baffle plate in between, that does not see high heat loads. The two horizontal targets are called low- and high-iota target plates. The high-iota target is primarily designed for the high iota configuration $\iota = 5/4$, whereas the low-iota target accommodates the heat and particle fluxes in the standard and low-iota cases. The toroidal bootstrap current produces a poloidal magnetic field, which changes the island size and can therefore influence the position where the island edge intersects the target.

## 3.4 Scrape-off Layer

In order to confine heat and particles the toroidal flux surfaces discussed above are nested. Adjacent to this confined region is the so-called Scrape-Off Layer (SOL) region. The last-closed flux surface (LCFS) or separatrix separates the two regions. The transport in the SOL is very different from the confined plasma due to these open field lines, as particles and heat that move along these open field lines will intersect material surfaces at the targets. The parallel transport along field lines is very fast compared to transport across them. This makes the power and particle flux channels narrow features with the potential for very high flux densities at the target - potentially exceeding the material limits of around $10\,\frac{\mathrm{MW}}{\mathrm{m}^2}$ [3]. Understanding the plasma transport in the SOL is therefore

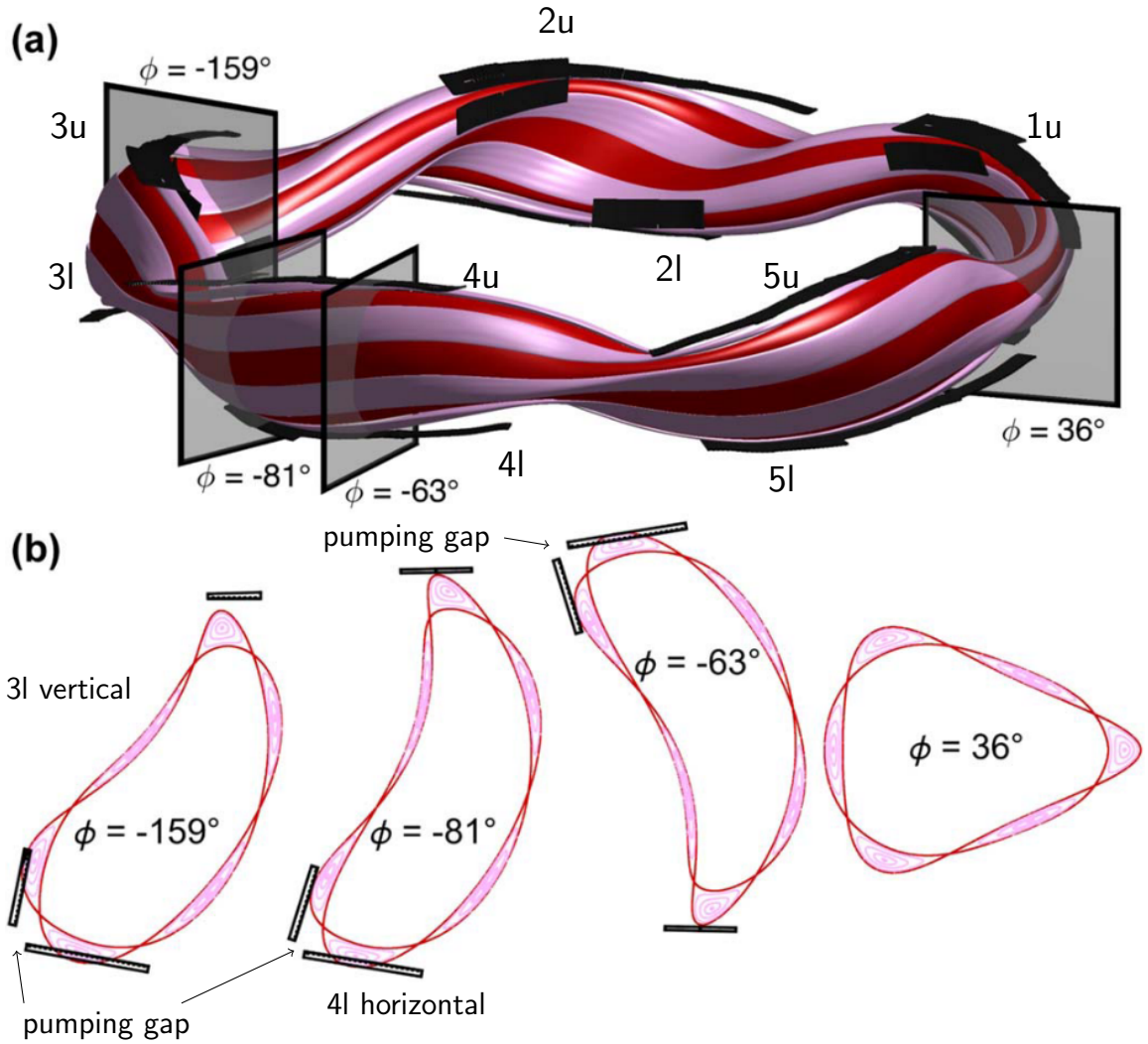


**Figure 6:** (a) Edge island (pink) and the last closed flux surface (LCFS) in W7-X for the low-iota magnetic configuration. The ten divertor targets are shown in black and labeled as 1-5u (upper) and 1-5l (lower)[18]. (b) Poincaré cross-sections at different toroidal angles $\phi$, corresponding to the planes in (a).

of utmost importance for designing a future fusion device. The targets and particle exhaust system must be designed such that impurity transport into the core plasma and heat load onto the target modules is reduced. By increasing strike line width and toroidal spread the wetted area is increased and heat-flux density onto the targets is reduced. Due to stellarator geometry, the W7-X SOL is inherently three dimensional. Because of this, the transport mechanisms differ from those observed in tokamaks [18]. The field line connection length $L_c$ is the distance along the field line from one target to the other target through that point. The SOL connection lengths in W7-X are in the order of hundreds of meters and are much longer than those seen in similar sized tokamaks, which are tens of meters. There are four main topological regions in the SOL, which can be distinguished by differences in $L_c$: the SOL, confined O-point region, target shadowed region (TSR) and the private flux region (PFR), which outside the island. Each of these regions are magnetically separated from each other, so transport can only cross between them via perpendicular transport. The later discussion is done for the low-iota configuration, so this case is discussed here. A map of connection lengths in the different regions inside the island at the toroidal angle $\phi = 36\,\mathrm{deg}$, obtained by field line tracing, is shown in fig. 7. From this, different regions in the island can be identified, see fig. 8. The island

SOL has direct and broad contact with the main confined plasma and has the longest connection length with $L_c = 450 - 1700\,\mathrm{m}$, which corresponds to multiple toroidal turns. The connection length is largest at the separatrix, where the parallel heat exhaust channel is formed due to the flux-surface perpendicular heat-flux that enters the island SOL from the confined region. The PFR is outside the island and only contacts the main plasma at the X-points. The target shadowed region (TSR) is the part of the SOL with short connection length, where field lines end on the target on both sides. It is subdivided further, into the lower-target shadowed region (LTS) and upper-target shadowed region (UTS), depending on which target cuts the island. In the outer shadowed region (OS) both upper and lower targets intersect the island. The island O-Point is a region of confined plasma inside the island.[19]

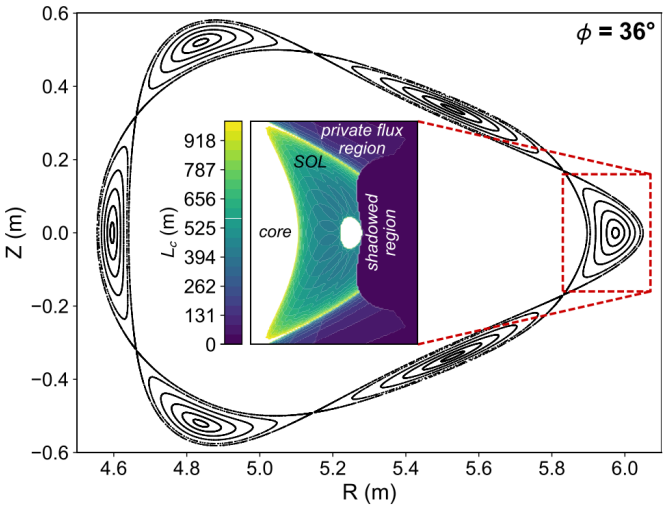


**Figure 7:** Poincaré cross-section of the edge island in the W7-X low-iota configuration. At $\phi = 36°$, the island is not intersected by targets. The connection lengths inside the island are also shown and the main topological regions are labeled [18]
.

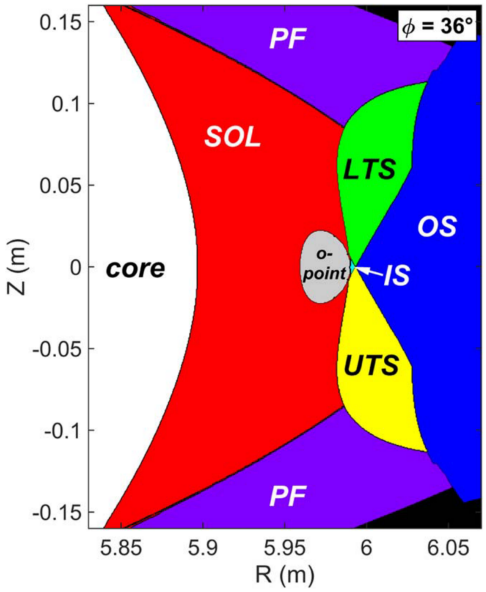


**Figure 8:** The different topological regions in the same setup as fig. 7. Additionally shown is a subdivision of the shadowed region into the lower-target shadowed region (LTS), upper-target shadowed region (UTS), inner shadowed region (IS) and outer shadowed region (OS) [18]
.

## 3.5 Heat Transport

This section discusses the major transport mechanisms for the heat in the SOL. Both conduction and convection, as well as drifts arising from electric fields in the plasma, facilitate heat transport to varying degrees. Two directions, parallel and perpendicular to the magnetic field **B** are discussed separately.

### 3.5.1 Parallel Transport

The flows parallel to **B** in the SOL are a connecting mechanism between sources and sinks, where the sinks are the divertor target plates. The dominant heat source comes

from cross-field diffusion from inside the LCFS due to heat deposition within the confined region. Power transport takes place primarily parallel to the magnetic field lines. This can be described as a 1D fluid conservation equation. It is here assumed that $E$ and $B$ are parallel, so no drifts occur. Drifts are discussed in section 3.5.2. Parallel power transport $q_\parallel$ $[\frac{\mathrm{W}}{\mathrm{m}^2}]$ in the SOL consists of conduction $q_{\parallel\mathrm{cond}}$ which is governed by coulomb collisions and convection $q_{\parallel\mathrm{conv}}$:

$$\begin{aligned} q_\parallel &= q_{\parallel\mathrm{cond}} + q_{\parallel\mathrm{conv}} \\ q_{\parallel\mathrm{cond}} &\approx -\kappa_e \cdot \frac{\mathrm{d}T}{\mathrm{d}s_\parallel} \\ q_{\parallel\mathrm{conv}} &= (\frac{1}{2}mv_\parallel^2 + 5k_bT)nv_\parallel. \end{aligned} \tag{7}$$

for Spitzer-Härm conductivity and convection [8, 20], where $\kappa$ is the electron heat conductivity given by $\kappa_\mathrm{e} \approx en_e v_\mathrm{e}\lambda_\mathrm{e} \approx 2 \cdot 10^3 \cdot T_\mathrm{e}^{5/2}$ and $s_\parallel$ the path along the magnetic field line. The thermal velocity of the electrons is $v_\mathrm{e} = (kT_\mathrm{e}/m_\mathrm{e})^{1/2}$ with the electron collisional mean free path $\lambda_\mathrm{te} = v_\mathrm{te}/\nu_\mathrm{te}$ where $\nu_\mathrm{te}$ is the collision frequency of thermalised electrons. As a result of $q_{\parallel\mathrm{cond}} \sim T^{5/2}$ scaling, conduction dominates at higher temperatures. Additionally, this means that the upstream temperature is very robust, depending only weakly on $q_\parallel$ or any other parameters. Even large changes in $q_\parallel$ are accommodated by a small change in temperature. Due to the mass difference of ions and electrons the main contribution to the heat conductivity comes from the electrons:

$$\frac{\kappa_e}{\kappa_i} = \sqrt{m_\mathrm{e}/M_\mathrm{i}} \approx 45. \tag{8}$$

The fast electrons in the tail of the thermal distribution with velocities of $v_\mathrm{hce} \geq 3.7 v_\mathrm{th,e}$ provide most of the conduction. This is because the collision frequency $\nu_\mathrm{e} \propto v_\mathrm{e}^{-3}$, which means $\lambda_\mathrm{e} \propto v_\mathrm{e}^4$, so hotter electrons are much less collisional than colder ones. The mean free path of a test particle of these heat conducting electrons $\lambda_\mathrm{hce}$ compared to the mean free path of Maxwellian target particles $\lambda_\mathrm{e}$ with the mean energy $mv_\mathrm{hce}^2/2 = 3/2k_BT$ is given by [21]

$$\lambda_\mathrm{hce} = (v/v_\mathrm{hce})^4\lambda_\mathrm{e} = (v/(\sqrt{3}v_\mathrm{th,e}))^4\lambda_\mathrm{e}. \tag{9}$$

This gives

$$\lambda_\mathrm{hce} = 21\lambda_\mathrm{e}. \tag{10}$$

This only holds at high collisionallities, where $\lambda_\mathrm{hce}$ is smaller than other system scales like the electron temperature gradient length and the length to the nearest solid surface. For this reason it is convenient to assume the conduction-limited regime, which can be done for higher density W7-X scenarios. The conduction is limiting and there are steep temperature gradients along the flux tube. Additionally, because of high collisionality between ions and electrons $T_e = T_i = T$ can be assumed. Because the influence of convection is small, ionisation of recycled particles only occurs close to the target surface, so flow effects including convection are only important in a thin layer close to the target, called the sheath. Across this region the ion velocity $v_i$ transitions from 0 to the plasma sound speed. $m_iv_i^2$ increases from 0 to $2k_BT$ at the target. Since $p = nk_BT$, the upstream pressure drops by half to the target $p_\mathrm{target} = \frac{1}{2}p_\mathrm{upstream}$. The formation of parallel temperature gradients is largely influenced by the ratio of heat-flux to particle flux density. In the conduction limited regime all of the power $P_\mathrm{SOL}$ enters the SOL at the upper end and is conducted along $s_\parallel$ for length $L$ to the target, where it is removed via the sheath. In this case we have a constant temperature and thus a constant parallel heat conductivity,

given by $\kappa_e = \kappa_0 \cdot T_e^{5/2}$. We thus get

$$q_{\parallel\mathrm{cond}} = (P_{\mathrm{SOL}}/A_{q\parallel}) = -\kappa_0 T^{5/2} \frac{\mathrm{d}T}{\mathrm{d}s}, \tag{11}$$

where $A_{q\parallel}$ is the total cross-sectional area of the power carrying channel and is therefore perpendicular to $\mathbf{B}$. Integrating equation 11 from $s_\parallel = 0$ to $L$ gives

$$T(s_\parallel) = \left[ T_u^{7/2} - \frac{7}{2} \frac{(P_{\mathrm{SOL}}/A_{q\parallel}) s_\parallel}{\kappa_0} \right]^{2/7} \tag{12}$$

for the temperature with the upstream temperature $T_u$ and the target temperature:

$$T(s_\parallel) = \left[ T_u^{7/2} + \frac{7}{2} \frac{(P_{\mathrm{SOL}}/A_{q\parallel})(L - s_\parallel)}{\kappa_0} \right]^{2/7}. \tag{13}$$

Assuming a significant temperature drop $T_u \gg T_t$, $T_t$ can be neglected because of the large exponent involved. We can then solve these two equations for $T_u$, resulting in

$$T_{\mathrm{u}} \simeq \left[ \frac{7}{2} \frac{(P_{\mathrm{SOL}}/A_{q\parallel}) L}{\kappa_0} \right]^{2/7}. \tag{14}$$

Calculating $T_u$ for a different case where the heat-flux is entering the transport channel not at the top, but uniformly along L, gives

$$T_{\mathrm{u}} \simeq \left[ \frac{7}{4} \frac{(P_{\mathrm{SOL}}/A_{q\parallel}) L}{\kappa_0} \right]^{2/7}, \tag{15}$$

which is different from eq. (14) by a factor of $(1/2)^{7/2} \approx 0.82$. This shows how insensitive $T_{\mathrm{u}}$ is to parameter changes, thanks to the high parallel heat conduction via fast electrons [2, 6, 20].

### 3.5.2 Drifts

Gradients of electric potential arising from different mechanisms cause drifts. Relevant drifts are the $\mathbf{E} \times \mathbf{B}$ drift

$$v_{\mathbf{E}\times\mathbf{B}} = \frac{\mathbf{E} \times \mathbf{B}}{B^2} \tag{16}$$

and the diamagnetic drift

$$v_{\mathrm{dia}} = -\frac{\nabla p \times \mathbf{B}}{(qnB^2)}. \tag{17}$$

The $\mathbf{E} \times \mathbf{B}$ drift can be split into a radial and a poloidal component.

The *poloidal* $\mathbf{E} \times \mathbf{B}$ *drift* is driven by the radial electric field: $v_{\mathrm{pol}} = E_r/B$. Near the conductive target plates, electrons, which are lighter than the ions, will leave the plasma more quickly. This charge imbalance forms a potential at the plasma wall called Debye sheath. The potential drop at the target is $\Phi \sim 3T_{\mathrm{e}}(r)/e$, leading to the radial electric field $E_r = \frac{\partial \Phi}{\partial r} \approx \frac{3T_{\mathrm{e}}}{e\lambda_{T_{\mathrm{e}}}}$, where $\lambda_{T_{\mathrm{e}}} = \left( \frac{1}{T_{\mathrm{e}}} \frac{\partial T_{\mathrm{e}}}{\partial r} \right)^{-1}$. The electron temperature $T_{\mathrm{e}}$ decreases in the island radially between the core plasma and the O-point, so $E_r$ points radially outward. In the PFR, $T_{\mathrm{e}}$ decreases moving radially away from the separatrix towards the

target [22]. Thus, inside the island $E_r$ points away from the separatrix and towards the O-point [19].

From the derivative of the planar sheath equation the Bohm sheath criterion is obtained. It states that for the ion velocity $u_s \geq \sqrt{k_B T_e / m_i}$ applies, where $k_B$ is the Boltzmann constant and $m_i$ the ion mass. If the ions are entering the Debye-sheath too slowly, the potential will start to extend into the plasma and accelerate them. This will develop the so called pre-sheath with a potential drop of $\sim k_B T_\mathrm{e}/2e$. The *radial* $\mathbf{E} \times \mathbf{B}$ *drift* is generated by a combination of this pre-sheath electric field $E_\parallel$ and the toroidicity $\varepsilon = a/R$, which is the ratio of the minor radius $a$ and the major radius $R$. The potential gradient along a field line results in a poloidal potential difference between neighboring passes of the field line. This creates a poloidal electric field $E_\mathrm{pol} = \Theta^{-1} E_\parallel$. The island field line pitch $\Theta = B_\mathrm{pol}/B_\mathrm{tor}$ of the island represents the ratio of distance moved poloidally around the O-point and the distance moved toroidally by the field line. Its value is around 0.001 in W7-X. From this electric field $E_\parallel$ a drift $v_{E,r} = \Theta^{-1} E_\parallel / B$ is generated. The influence of Ohm's law [20] on $E_\parallel$ must also be considered:

$$E_\parallel = \frac{j_\parallel}{\sigma_\parallel} - \frac{0.71}{e}\frac{\partial T_e}{\partial s_\parallel} - \frac{1}{en}\frac{\partial p_e}{\partial s_\parallel}, \tag{18}$$

where $j_\parallel$ is the parallel current density, $\sigma_\parallel$ is the parallel electrical conductivity, $s_\parallel$ is the parallel distance, and $\frac{\partial T_\mathrm{e}}{\partial s_\parallel}$ represents the partial derivative of electron temperature with respect to parallel distance. At high temperature the conductivity, which scales with $\sim T^{7/2}$, is high and hence $E_\parallel$ is small for expected current density. Since $p \sim T$, $\frac{\partial T_e}{\partial s_\parallel}$ and $\frac{\partial p_e}{\partial s_\parallel}$ are dependent on the temperature gradient, which extends between the LCFS and the target. At higher densities, the gradient $\frac{\partial T_\mathrm{e}}{\partial s_\parallel}$ becomes larger, increasing radial transport $v_{E,r}$.

There are three sources of *diamagnetic drift*. The magnetization flux is divergence-free and therefore has no influence on plasma distribution. The curvature drift, which was also mentioned in section 3.2, and $\nabla B$ are not divergence free. They are however largely vertical and are therefore averaged out by the helical twist of the island chain [23], at least for mean field particle transport. They can however provide convective heat transport, which will be discussed in section 3.5.3. All drifts depend on the direction of the magnetic field. This can be used to discern drifts in the SOL by comparing upper and lower targets, as they break stellarator symmetry. $\mathbf{B}$ is in the same direction at the top and bottom divertors, so $\mathbf{B}$ is reversed with respect to the symmetry of the target.

### 3.5.3 Perpendicular Anomalous Transport

Turbulent transport is considered to be the main driver for cross-field transport in the SOL, and has convective and diffusive components. Convective turbulent transport can occur as individual filaments, which generally average out in the mean field approach over sufficiently long time scales, so their impact is overall diffusive. Even though neither the diffusion nor convection are able to uniformly describe the experimental measurements on their own [13, 24] describing perpendicular transport as diffusive gives reasonable agreement and is computationally advantageous. The total cross-field particle flux density $\Gamma_r$ is therefore often described with Fick's law of diffusive motion with an anomalous diffusion coefficient $D_\perp$ $[\frac{\mathrm{m}^2}{\mathrm{s}}]$:

$$\Gamma_r = D_\perp \frac{\partial n}{\partial r}, \tag{19}$$

where $(\frac{\partial n}{\partial r})$ is the radial density gradient. The flux $\Gamma_r$ generated by an initial concentration gradient will in turn change this gradient over time, thus $n(r,t)$. This process is governed

by Fick's second law

$$\frac{\partial n(r,t)}{\partial t} = D\frac{\partial^2 n(r,t)}{\partial r^2}. \tag{20}$$

which can be solved with the initial condition of a particle density $n_0$ at $r = 0$:

$$n(r,t) = \frac{1}{\sqrt{4\pi Dt}} \exp\left(-\frac{r^2}{4Dt}\right) \tag{21}$$

so n is proportional to a Gaussian distribution. In [13], a roughly linear relation of $\Gamma \sim \nabla p$ and therefore $\Gamma \sim \nabla T_\mathrm{e}$ was found for most W7-X cases. Perpendicular heat diffusion via conduction is discussed similar to parallel heat conductivity, which has the same mathematical form as eq. 19:

$$q_{\perp\mathrm{cond}} = -n_\mathrm{e}\chi_\perp \frac{\mathrm{d}T}{\mathrm{d}r} \tag{22}$$

switching $D_\perp$ with the perpendicular heat diffusivity $\chi_\perp$ times the electron density $n_\mathrm{e}$.

Turbulent convective particle transport perpendicular to $B$ arises due to small-scale fluctuations, which can not be accounted for entirely by classical collisional effects [6]. Electrostatic fluctuations of plasma density $\tilde{n}$, electron temperature $\tilde{T}_\mathrm{e}$ and electric potential $\tilde{V}$ are the main drivers, whereas magnetic fluctuations play a minor role for SOL transport [25]. $T_e$ fluctuations are also being neglected here, since experiments at W7-X have shown that they are usually small and approximately in phase with the potential fluctuations [26].

Here considered is perpendicular particle transport in the case of a plasma in a magnetic field $\mathbf{B}$ and a density gradient $\nabla\bar{n}$ perpendicular to $\mathbf{B}$. Given a background density $< n >$ with a perturbation $\tilde{n}$ perpendicular to $\mathbf{B}$ and $\nabla\bar{n}$, this plasma density perturbation $\tilde{n}$ will be in equilibrium with a perturbed electrostatic potential field $\tilde{V}$, according to the linearized Boltzmann relation:

$$\frac{\tilde{n}}{n} = e\tilde{V}/k_\mathrm{B}T_\mathrm{e}. \tag{23}$$

This results in a perturbed $\tilde{E}$-field, which then results in a cross-field $\tilde{\mathbf{E}} \times \mathbf{B}$ drift in the direction of the density perturbations $\nabla\bar{n}$ (see section 3.5.2), changing the density perturbations $\tilde{n}$.The perturbations become a drift wave, moving perpendicular to $\mathbf{B}$. This is in the same direction as the electron diamagnetic drift. Electric currents are also generated perpendicular to the magnetic field due to polarisation and diamagnetic drifts.

## 3.6 Transport inside the SOL

For practical purposes, three different transport mechanisms are being differentiated (fig. 9). Heat and particles enter the island across the LCFS. Local particle sources from ionization inside the SOL are ignored here. *Parallel transport* is primarily convective (at higher densities) as discussed in section 3.5.1. The heat-flux follows the magnetic field lines, moving along the island flux surface with each toroidal turn. *Binormal transport* is perpendicular to both the parallel direction and the radial direction. It includes poloidal drifts and diffusion. It leads to heat-flux skipping toroidal turns, so that the LCFS is topologically closer to the target. The particle and heat-flux is directed either to the left in fig. 9, where it hits the target as the strike line, or to the right into the TSR, from where it is transported onto an upper target with very short connection lengths. Depending on the poloidal $E \times B$ drift the stagnation point is moved left or right, changing the amount of heat-flux into the TSR [19]. Inside the island the flux surfaces are also more or less isothermal, creating a temperature and therefore pressure gradient perpendicular to the island flux surfaces. Particles and heat are also transported radially towards the O-point, out of the power carrying layer, forming a shortcut onto the target. Behind the X-point perpendicular diffusion occurs from the island edge into the island, but also into the PFR outside the island. In the PFR the connection lengths are much shorter than inside the island, so a significant thermal gradient is created here.

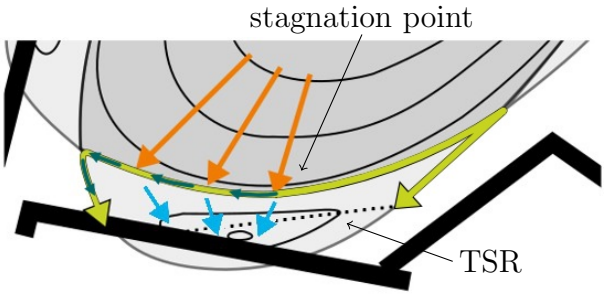


**Figure 9:** Schematic depiction of parallel- (light green), binormal- (dark green) and radial perpendicular (blue) transport in the island at the target. The island area under the dotted line is the TSR. Heat-flux from the core is shown in orange. Adapted from an illustration by Dr. Valeria Perseo.

## 3.7 Heat-flux Profile

For modeling the upstream heat-flux profile an exponentially decaying power profile at the boundary between island and the confined plasma is assumed:

$$q_{\exp}(s) = q_0 \cdot \exp\left(-\frac{x}{\lambda_q}\right), \tag{24}$$

where $q_0$ is the upstream peak heat-flux, $x$ the radial distance from the LCFS, and $\lambda_q$ the power fall-off length. It comes from the interplay of the strong parallel drainage towards the target and the perpendicular diffusion in flux-surface perpendicular direction towards the o-point. On top of this, perpendicular diffusive heat transport is assumed, as the heat transports along the field line towards the target. Equation 24 is therefore convoluted with a Gaussian:

$$q_{\parallel}(s) = \frac{q_0}{2} \exp\left(\left(\frac{S}{2\lambda_q}\right)^2 - \frac{s - s_0}{\lambda_q \cdot f_x}\right) \operatorname{erfc}\left(\frac{S}{2\lambda_q} - \frac{s - s_0}{S \cdot f_x}\right), \tag{25}$$

where $f_x$ is the poloidal flux expansion caused by geometric effects, which is the ratio of the width of a flux surface downstream to upstream. $s$ is the position on the target and $s_0$ the position of the island separatrix on the target. Before the X-point $q_{\parallel}$ decays

exponentially with parameter $\lambda_q$. After the X-point, perpendicular transport via diffusion carries heat-flux into the PFR in one direction and broadens the strike line in the other. The broadening can be described by a broadening parameter $S$ defined by the ratio of perpendicular to parallel transport:

$$S \sim L\sqrt{\frac{\chi_\perp}{\chi_\parallel}}, \tag{26}$$

where L is the connection length between the X-point and the divertor target, $\chi_\perp$ the heat diffusivity perpendicular and $\chi_\parallel$ parallel to the magnetic field lines. Note here that this simple tokamak model does not consider the complex stellarator geometry or any dissipative processes. [1]

## 3.8 SMoLID

The Simple Model for Loads in Island Divertor (SMoLID) is a new not yet published tool by Amit Kharwandikar, that is able to predict heat load onto the target. It uses the idea introduced in the previous section of a power carrying layer (PCL) with fast parallel transport and in addition exponential decay:

$$q_{\mathrm{target}_{i,j}} = q_{\parallel \max} \exp\left(-\frac{\Delta_{i,j}}{S_\perp}\right) \cdot \sin \alpha_{i,j} \tag{27}$$

where $\Delta$ is the minimum perpendicular distance of an target area element $(i, j)$ from the PCL. The perpendicular transport is parameterized as the length scale $S_\perp$ signifying power spreading, similar to eq. 26. $\alpha$ is the inclination angle of the magnetic field at area element $(i, j)$. The assumption is made that the PCL carries the constant heat-flux $q_{\parallel \max}$. Radial perpendicular transport and binormal transport both transport heat away from the power caying layer. Binormal transport introduces a poloidal leakage of heat-flux into adjacent topological regions. Radial perpendicular transport leads to broadening of the power channel towards the o-point. They are treated independently with $S_{\perp r}$ and $S_{\perp b}$. The scaling factor $q_{\parallel \max}$ needs to be determined by fitting the IR-data, for which the fitting routine developed in this work might be used for in the future.

# 4 Methods

## 4.1 Experimental Scenarios

To study SOL transport, it is necessary to use W7-X experiments with low radiation fraction, so that the transport is prominent and easier to study. For this analysis two sets of three W7-X experiments have been chosen. The experiments in the standard configuration #20180920.009, #20180920.013 and #20180920.017, which have also been used by [4], are part of a density scan with an input power of 4.7 MW ECRH and line integrated densities $\int n_e$ of 4, 6 and $8 \cdot 10^{19}\,\mathrm{m}^{-3}$. The total heat-flux on the divertor measured by the IR-diagnostic was 3-4 MW, shown in fig. 10b. The toroidal current increased to around $I_{tor} \approx 5\,\mathrm{kA}$ at 6 seconds. For time averaged analysis the time interval from 2-4 seconds has been used in all six experiments. A density scan in the low iota configuration has also been analysed with experiments #20180829.009, #20180829.017 and #20180829.026. For transport analysis the low iota configuration has a number of advantages, including its relative insensitivity to resonant error fields that would otherwise deform the edge islands and convolute the drift contributions to the asymmetric charge patterns. Low iota also has the longest connection lengths and smallest internal field line pitch of any of the main W7-X configurations, thereby maximizing the impact of drifts on SOL transport. In general, power onto the target decreases with increasing density, which is to be expected, as with increasing density the radiation fraction increases, reducing target heat load. The strike line moves over time with increasing plasma current, as seen in fig. 10. Since the relationship between current and strike line movement is linear in first order, a simple linear regression over two seconds was used to determine the movement speed of each feature at each finger.

## 4.2 IR-Mesurements

To analyse the divertor power deposition, a thermographic diagnostic system is used. Nine immersion tubes with infrared cameras are installed, recording nine of the ten divertor units with a frame rate of 100Hz in a wavelength range of 8-10 µm. The camera data is mapped onto a 2D plane for better analysis. With the help of the THEODOR code a 2D heat diffusion equation is solved numerically for the target fingers [27]. With this, the heat-flux onto the target can be re-constructed from the IR-emissivity of the target surface, resulting in a high resolution map of the heat-flux onto the target. The method for the processing of the camera data can be found in detail in [3].

## 4.3 Target Geometry Parametrisation

The divertor targets are positioned on each side of the pumping gap as shown in fig. 12. Each divertor is build from a series of consecutive thermally isolated target elements called divertor fingers. The target geometry is mapped from its 3D-shape (fig. 12) to a flat 2D array (fig. 13). The divertor finger modules are named based on their location upper (u) or lower (l), vertical (v) or horizontal (h) and the reactor module number. Finger module number 4 at reactor module number 2 on the lower horizontal target is therefore called 2lh_4. The coordinate map_x is roughly aligned with the magnetic field, while map_y is roughly orthogonal to the magnetic field. Each finger consists of a solid block of carbon, except some of the fingers which are made of tungsten for the study of Plasma wall interactions (PWI). The heat-flux calculation is not applicable for these fingers due to the complex surface layers which have been prepared on the marker tiles for material

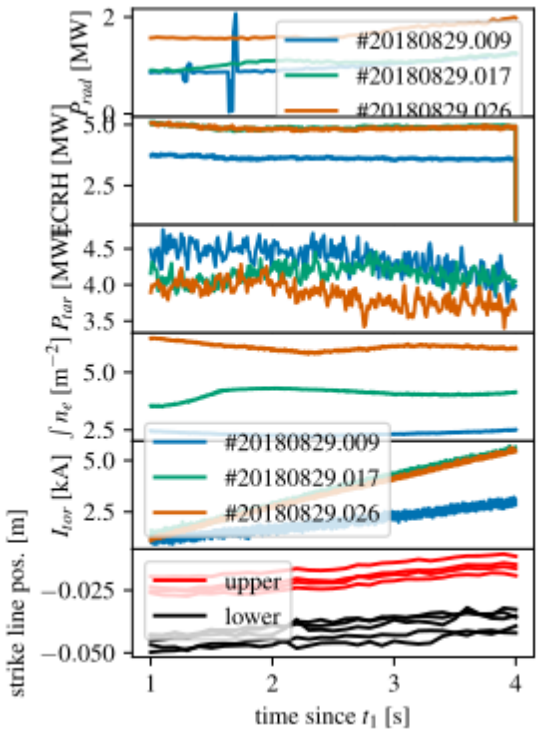


**(a)** The low iota configuration experiments #20180829.009, #20180829.017 and #20180829.026.

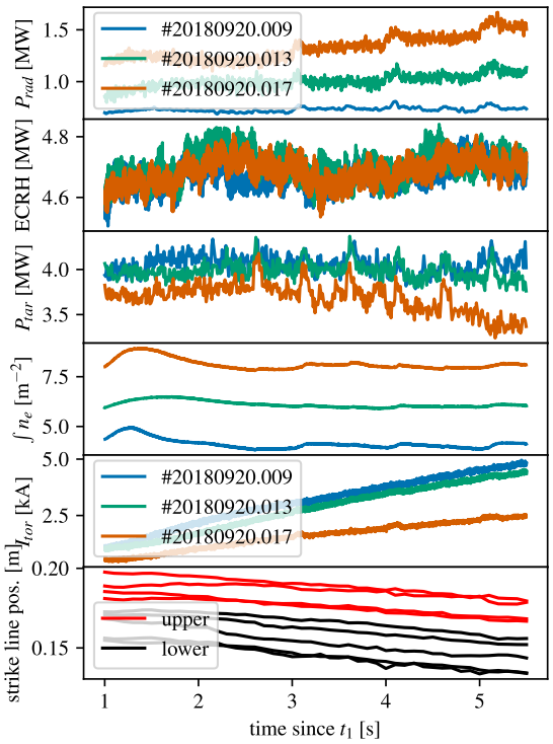


**(b)** The standard configuration experiments #20180920.009, #20180920.013 and #20180920.017.

**Figure 10:** Overview of the time evolution of the radiated power $P_{\mathsf{rad}}$, the ECRH heating power, the power on the target measured by the infrared diagnostic IR, the line integrated density $\int n_{\mathsf{e}}$, the toroidal plasma current $I_{\mathsf{tor}}$ and the strike line position for each target on finger 24.

studies. Therefore these tiles must be excluded from the analysis [3]. Also not included are the 5u and 5l divertor modules.

## 4.4 Method of Heat-flux Parametrisation

For this analysis each divertor target finger is split into several 1D slices, representing the strike line profile. The heat-flux data is then mapped such that the axis are approximately perpendicular to the magnetic field lines as shown in fig. 13. The data is averaged over ten frames so each time step is 100 ms). Each profile is then fitted with a function consisting of multiple Gaussian curves, as done in [4]. As described in 3.7, the model assumes diffusive heat transport perpendicular to the flux surfaces. Except for regions with short connection lengths, the diffusive perpendicular heat transport is strong enough that the strike line can be assumed to be shaped like a Gaussian. Contrary to [4], the number of Gaussians is not fixed, but is determined beforehand via a peak detection. This is done in three steps, shown in fig. 11, to most accurately capture all the features present in the strike line profile. First, initial values for a narrow and broad Gaussian are chosen, and the fitting routine is run. The height and position of the narrow Gaussian is that of the global maximum in the fitting data. The width is determined by the peak detection algorithm. The height of the broad Gaussian is set at 1/4 of the narrow Gaussian and its width is set at 1/3 the range of the x-axis. A custom loss function is used, where the residual for a point above the fit is increased tenfold. This ensures that the initial fits are

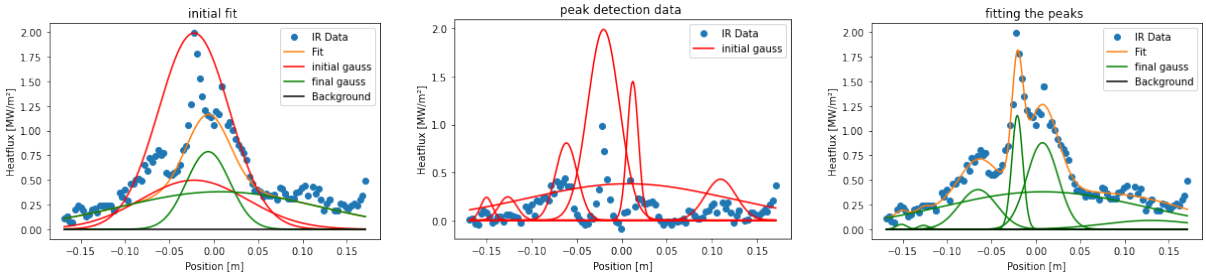


**(a)** First, initial values for a narrow and broad Gaussian are chosen (red), and the fitting routine is run (green). A custom loss function is used, where the residual for a point above the fit is increased tenfold. This ensures that the initial fits are below the data, so any perturbations from the Gaussians are above the fit.

**(b)** The fit from a) is subtracted from the measured data and the peak detection is run. Each additional perturbation gets its own Gaussian. The initial height is obtained from the original data.

**(c)** With the initial values from b) the original data is fit, this time with a euclidean loss function.

**Figure 11:** The three fitting steps for an example heat-flux profile. Shown is the sum (orange) of all Gaussians (green) together with the fitting data (blue). The 0-point on the x-axis is the mid-point of the target finger.

below the data, so any perturbations from the Gaussians are above the fit. Thereafter the fit from fig. 11a is subtracted from the data and the peak detection is run. Each additional perturbation gets its own Gaussian. The initial width and height are obtained from the original data (fig. 11b). With the initial values the original data is fit, this time with an euclidean loss function, so that the fit best approximates the data. The routine is run for all time steps and slices. Especially for more complicated profiles multiple ways to fit the data are possible, resulting in sometimes very different structures between neighboring time steps or slices. This is why the resulting Gaussians are then clustered relating to their height, width and position using the Hierarchical Density-Based Spatial Clustering (HDBSCAN) algorithm of the scikit-learn library [28] to determine the most prominent fit structure. The Gaussians from two time steps in front and behind the current time step and all slices from one finger are clustered together, improving consistency greatly. The two slices next to the finger edge are not used, the reason is discussed at a later point. The resulting cluster centers are then used as initial fitting values for the whole finger in a second fitting iteration. Each fit is then evaluated using residuals. Only fits with sufficiently low residuals are kept. The Gaussians are clustered again, different features on each finger or slice can then be tracked over time via distance clustering.

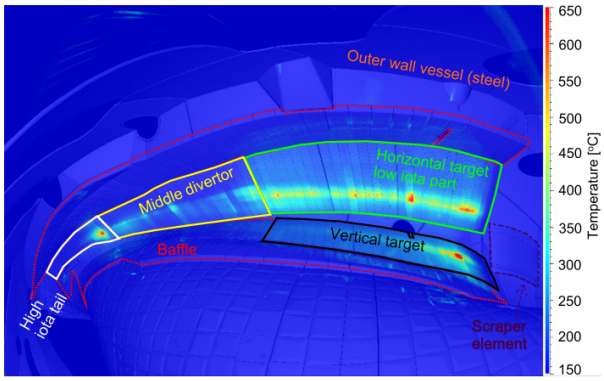


**Figure 12:** The distorted CAD model of the vessel overlaid by the surface temperature, reproduced from [3].

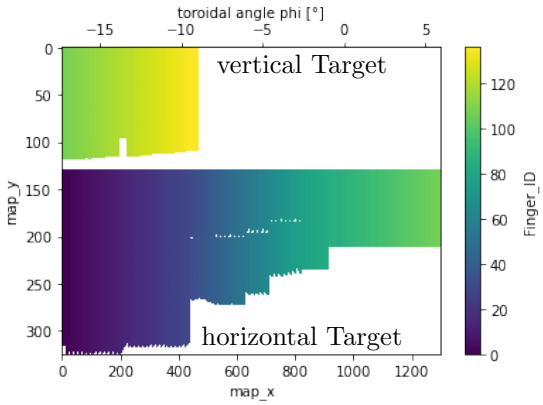


**Figure 13:** The view of the target, but mapped such that map_x is roughly aligned with magnetic field, while map_y is roughly orthogonal to the magnetic field. Each Finger consists of about 15 slices in map_x direction, where each slice is one map_x wide.

# 5 Results

## 5.1 Strike Line Parameters

The fitting results of the six discharges from the two density scans are are shown in figs. 18-23. For the low iota cases only the low iota target and part of the middle divertor are plotted, since no heat-flux is deposited elsewhere. For the standard configuration the whole divertor is shown, with the vertical target on the right side. The position on the target is expressed in terms of map_y, which has the advantage that features stay roughly at a constant map_y toroidally. The width is not the width of the wetted area, but the width of the Gaussian at half height. The connection length at the respective features position is produced from field line tracing. Features that have been identified as artifacts or deposits with low amplitude are shown in grey. The main strike is blue, with some noteworthy features colored differently. The data is averaged over the four upper and lower targets respectively. By toroidally plotting the connection length along the strike line, three topological regions can be differentiated. The border between target shadowed region and scrape off layer is at $\phi \approx -16°$. In low iota configuration, the width of the SOL footprint becomes very narrow with increasing map_x (fig. 26), making it difficult to determine a toroidal border. Even small deviations in map_y lead to big toroidal changes, which are to be expected because of the toroidal current and drift effects. However, around $\phi \approx -6.2°$ the heat flux starts to decrease exponentially, indicating the border to be there. The increased heat-flux from $\phi = -8°$ to $-6°$ might be due to the toroidal change in incidence angle, which influences target heat-flux (eq. 27). In fig. 14 an example result for the fitting routine described in section 3.5.1 is shown. The Gaussian's are clustered based on their distance in the 3D parameter space of position, width and amplitude. Sometimes Gaussians of the same time step are clustered together (fig. 14a). This is corrected in (fig. 14b). Notable features in the strike line profile in (fig. 14c) are the discontinuity at position $-0.2\,\mathrm{m}$, the main strike line at $-0.15\,\mathrm{m}$ and the small amount of heat-flux next to the strike line, which are all discussed in section 6.1. The heat-flux profile in fig. 17 for the low density case in fig. 18 is from $\Phi \approx -16°$. Heat-flux profiles from inside the target shadow region are not Gaussian shaped and unsymmetrical, which is why they are fitted with multiple Gaussians by the routine. The strike line amplitude does

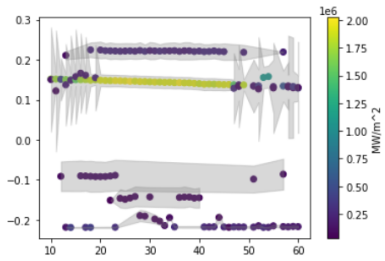

**(a)** Sometimes two Gaussian at the same time step are clustered together if they are similar enough.

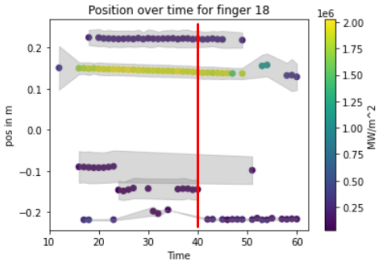


**(b)** Each feature is checked for multiple Gaussian at the same time step and the one closest in amplitude, width and position to the surrounding Gaussian is kept.

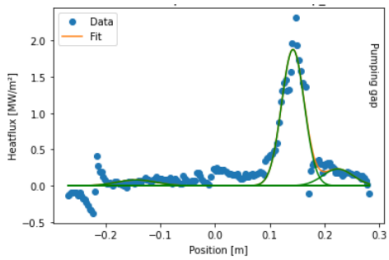


**(c)** The strike line profile at time step 40 (red line in (b)). The fitting profile is shown in yellow, the individual Gaussian in green.

**Figure 14:** (a, b) The Gaussian parameters height, width (grey) and position on the y-axis over time for finger module 1lh_18. This is after the initial clustering of the Gaussian's. (c) The strike profile at the time step 40 with the fitted Gaussian's. Shown is discharge #20180920.013.

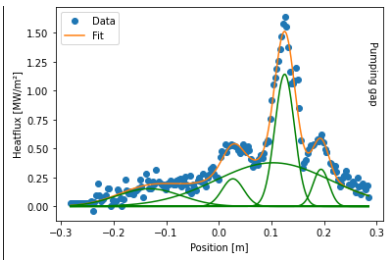


**Figure 15:** The strike line of discharge #20180920.017 at target finger 1uh_12 at time step 3 s. The heat-flux left and right from the strike line is the result of deposits on the target.

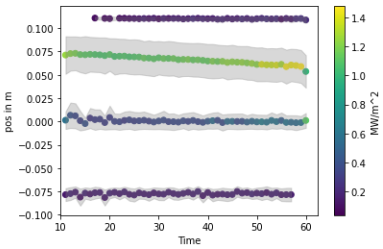


**Figure 16:** Discharge #20180920.017 at target finger 1lh_16. The strike line movement over time is in contrast to the surface features, which remain stationary.

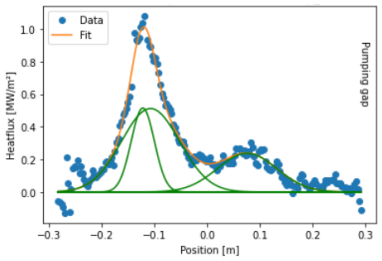


**Figure 17:** Low density discharge #20180829.009 at target finger 1lh_4 at 2.9 s. The strike line is not symmetric. The small amount of heat-flux on the right is the result of surface deposits on the target.

therefore not represent the actual maximum heat-flux. Additional charts with connection length maps are in the Appendix figs. 32 and 31. For the low iota cases, the strike line seems to be closer to the pumping gap than in the low density case fig. 26.

# 6 Discussion

## 6.1 Surface Features and Limitations

Before discussing plasma-related phenomena, it is important to consider the limitations arising from the recording and processing of the infrared data. For this discussion, low to medium density experiments have been chosen. At low densities the plasma strike line is narrow, whereas at higher densities the strike line widens. This can lead to overlap, making it difficult to identify features that are not directly related to the strike line. In fig. 24, the heat flux is shown for experiment #20180920.009 with the standard magnetic

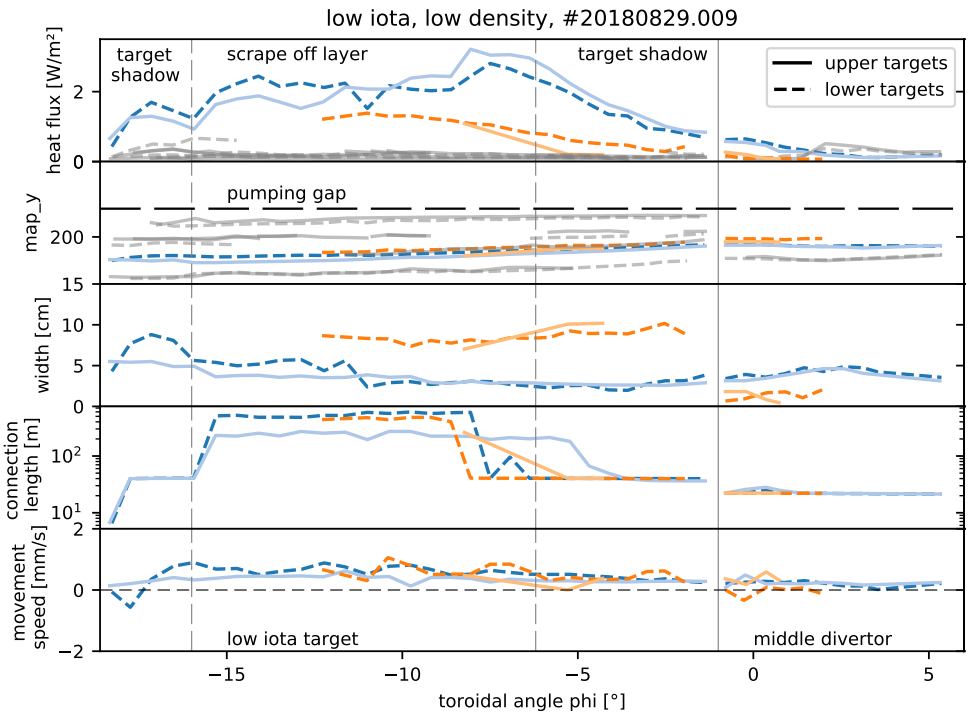


**Figure 18:** The Gaussians height, width and position. The main strike line is blue, an underlying broad feature is shown in orange.

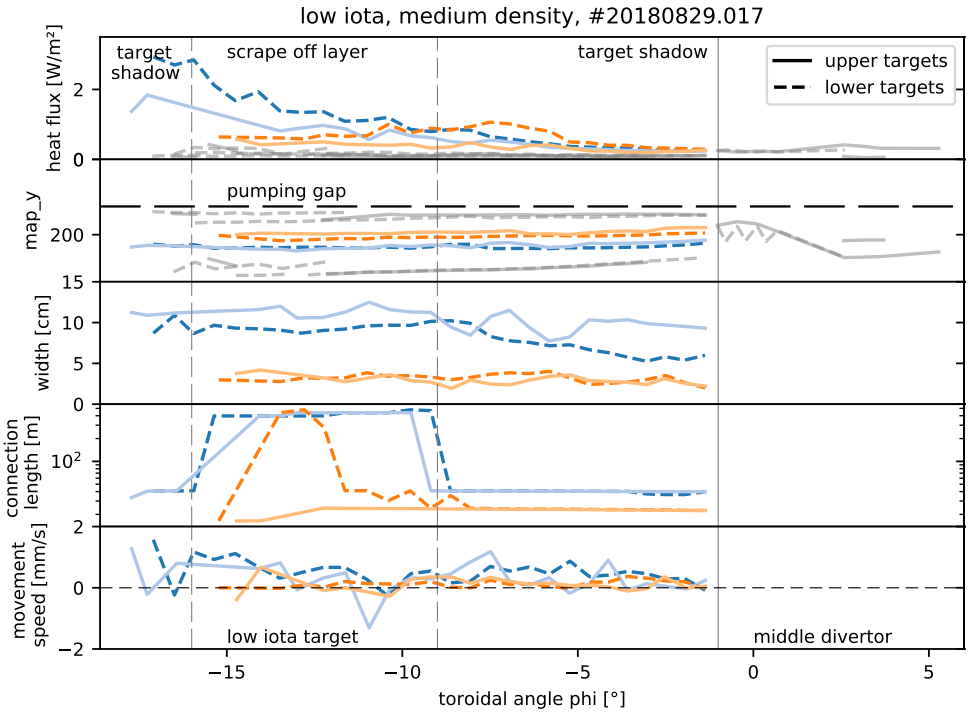


**Figure 19:** Contrary to fig. 18, the lower deposit (orange) and strike line (blue) are fitted independently. The wider strike line causes higher heat flux on the lower deposits at map_y $\approx 200$, which exceeds the main strike line at some regions.

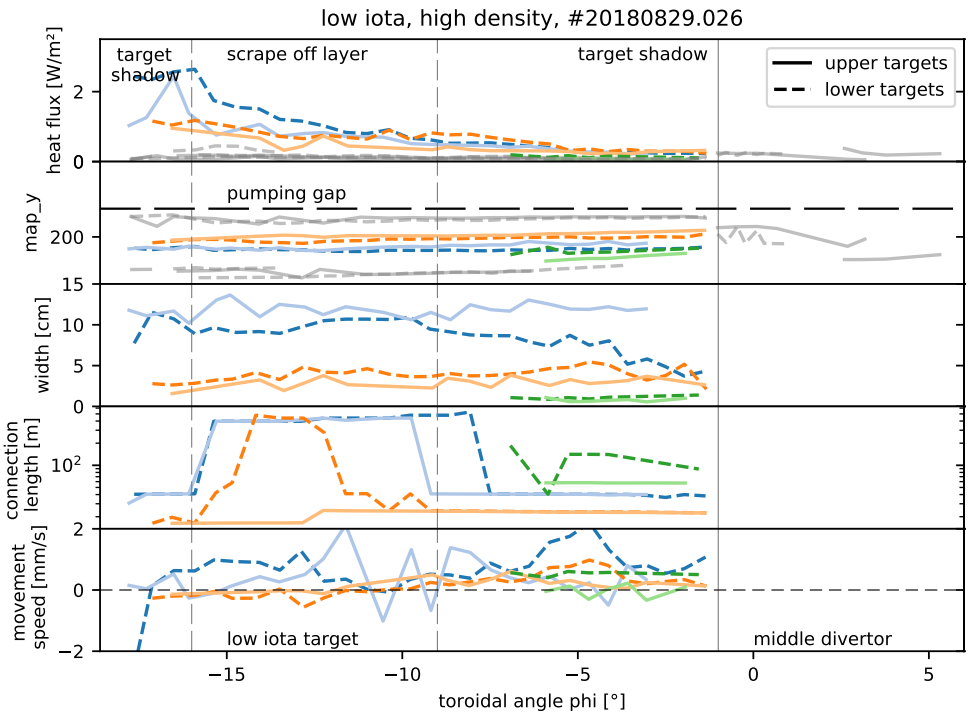


**Figure 20:** This discharge shows a similar behaviour to fig. 19, except for an additional narrow green feature.

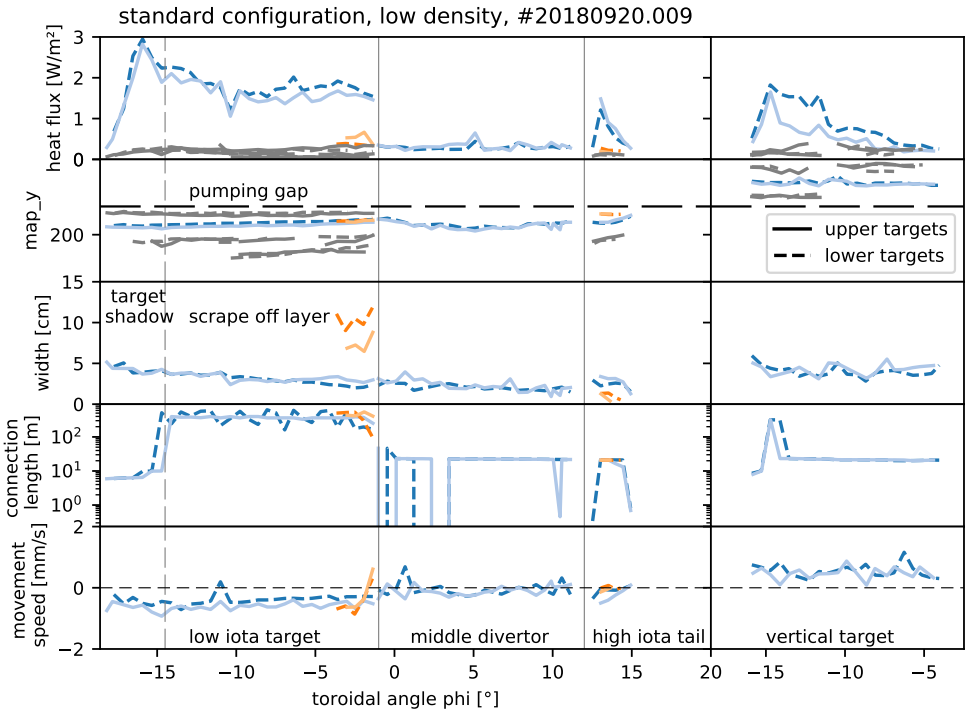


**Figure 21:** In the standard configuration each part of the divertor is loaded with heat-flux. Deposits and strike line have been fitted mostly independent of each other. The strike line on the middle divertor target seems to be stationary.

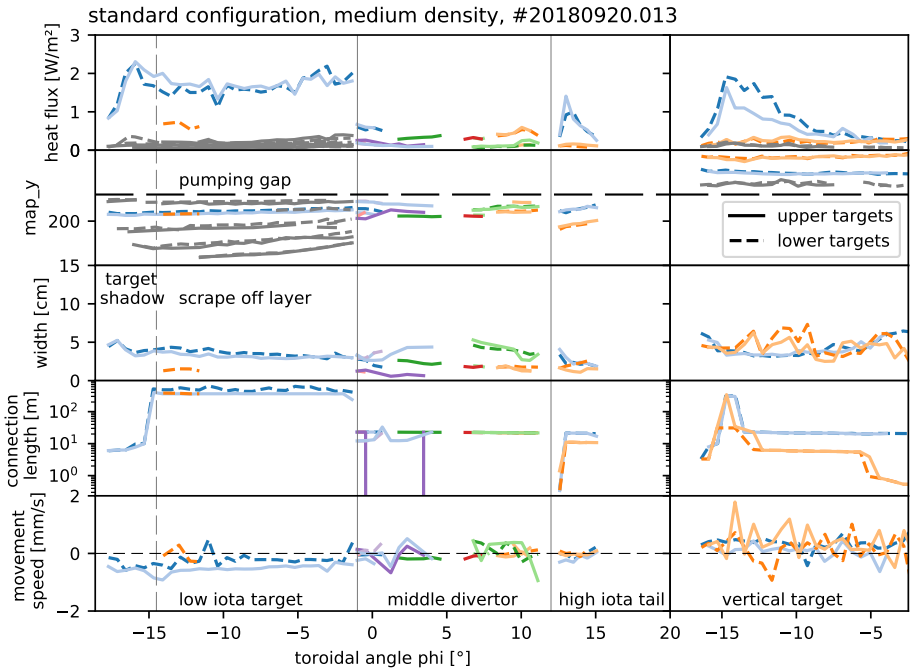


**Figure 22:** The heat-flux on the middle divertor target shows multiple features. On the vertical target the reflections are shown in orange.

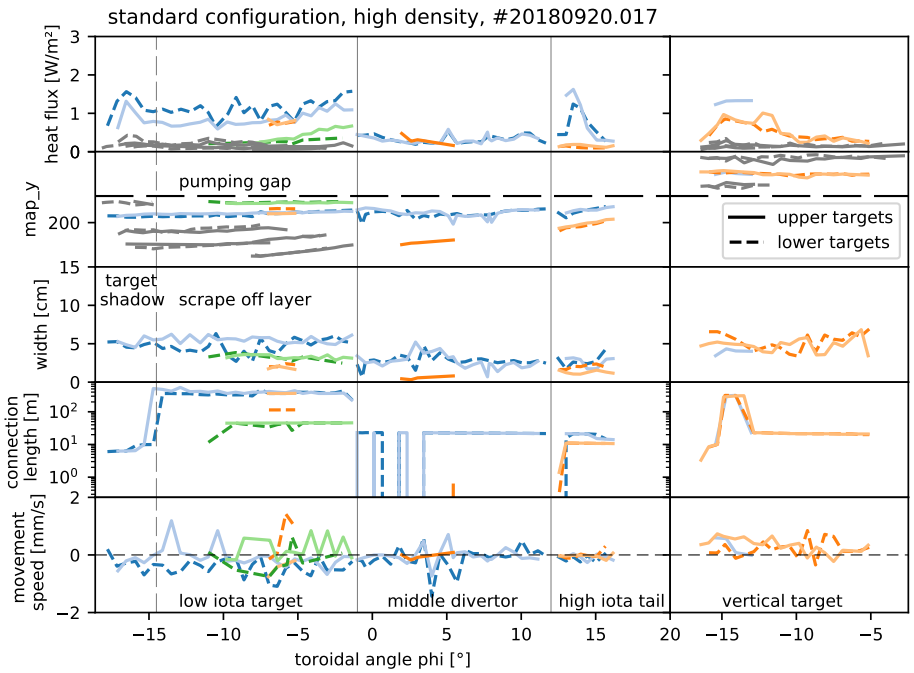


**Figure 23:** In this discharge a significant amount of heat-flux hits the upper deposit (green). The high variation in the movement speed compared to the lower density cases (figs. 21, 22) shows the inconsistency in determining the strike line position at higher densities.

configuration and #20180829.009 with the low iota configuration. Both are low density discharges, leading to a narrow strike line. Material that has been eroded inside the vakuum vessel is deposited onto the target, forming a thin layer of material which has poor heat conductivity to the underlying carbon block. This layer has a tiny thermal capacity, which is why the surface heats up almost instantly when hit with even small amounts of heat flux. This increased surface temperature leads to incorrect heat flux calculation in these deposition regions. Net deposition zones are mainly next to the strike line. In fig. 28, the darker deposition zones are clearly visible next to the lighter region, where the strike line has eroded the surface. Marked is the strike line position for the standard configuration. The low iota configuration has not been run often enough in OP 1.2 to leave clearly visible erosion on the target. Due to the lower thermal conductivity of the sputtered material, the deposits are also visible in the thermal imaging system in between experiments. Since they insulate the target surface, less thermal radiation is emitted as by surrounding regions. During plasma loading in the low iota configuration the deposition zones can be seen next to the net erosion zone around the standard configuration strike line. Due to reduced thermal contact deposition layers show higher surface temperatures and emissivity than would be expected on clean carbon fingers, which is seen in the heat flux data in fig. 24. Another source of additional IR-radiation flux that the analysis will interpret as increased temperature and heat flux, is reflection from other parts of the target. In W7-X, the influence of reflections can not be neglected, despite carbon targets having lower reflectivity than metal surfaces. Ray tracing simulations (figs. 30, 29) have shown that in the standard configuration a significant amount of radiation originating from the strike line on the horizontal target is being reflected onto the vertical target (fig. 25). In the low iota configuration no significant amount of radiation is expected. The high iota target is furthest from the camera which results in a lower resolution than other parts of the target. This bad visibility leads to blocking and inaccurate heat flux calculation. The camera view is blocked at the lower edge of the low iota target by the baffle tiles which surround the targets. This leads to a ridge in the IR-data that is fitted by the routine. This can be seen in the IR-data in fig. 25) and also as the bottom most feature in figs. 18, 19 and 20.

This discussion can be used to classify the different features on the target. Comparing the location of features on the target with the connection lengths in fig. 26, the position of deposits, artefacts (grey) can be separated from the strike line (blue) in figs 18-23. The broad feature (orange) in fig. 18 is interpreted to likely be the lower of the two surface deposits and part of the main strike line, which are sometimes fitted individually and sometimes together as a broad feature by the fitting routine. At higher densities, the strike line is much broader at around 10 cm shown in fig. 19 for a line integrated density of $\int ndl = 4 \cdot 10^{19}\,\mathrm{m}^{-2}$ and fig. 20 with $\int ndl = 6 \cdot 10^{19}\,\mathrm{m}^{-2}$. Here the deposit at map_y $\approx 200$, shown in orange, is being loaded with plasma from the broader strike line, which increases their IR-emissions as discussed in 6.1. In fig. 20 with higher density the lower deposit receives enough heat-flux that its IR-radiance is at some points higher than the main strike line. This is of great concern, since the strike line position and amplitude are generally determined by the heat-flux maximum. The power, which is the area under the heat-flux profile, is also overestimated in the affected cases.

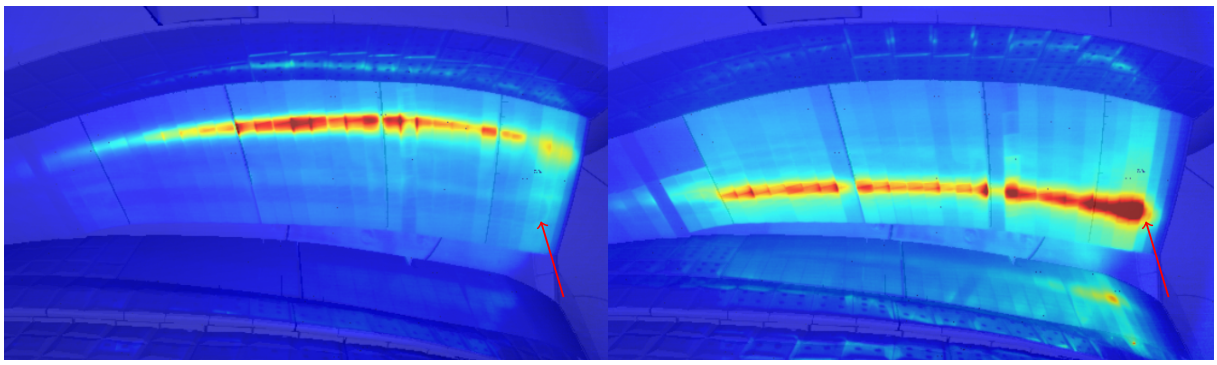

**Figure 24:** In the low iota configuration (left) the deposits left and right outlining where the strike line (red) hits in the standard configuration (right) leading to increased IR surface emission. The data was kindly provided by Dr. Marcin Jakubowski.

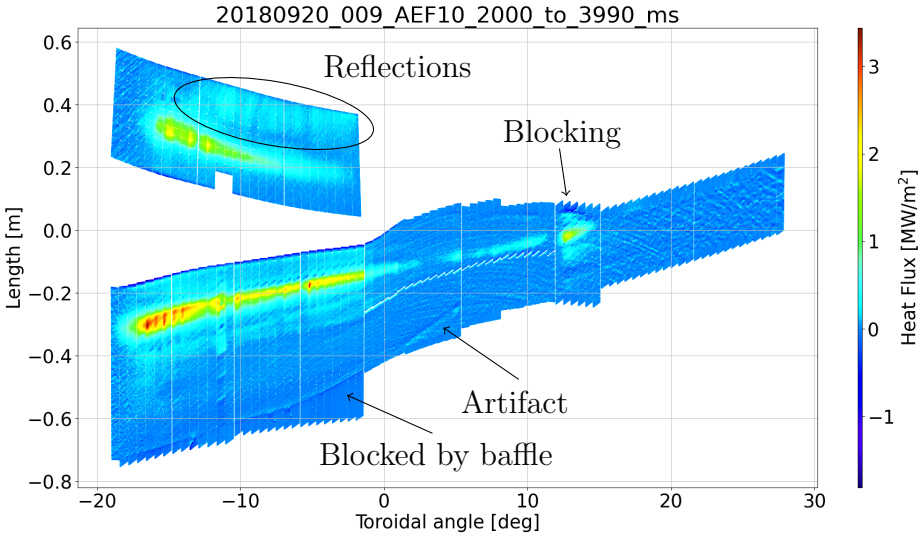


**Figure 25:** Shown here is discharge #20180829.009 in the standard configuration with low density and therefore narrow strike line. Marked are features of interest, kindly provided by Dr. Yu Gao. IR radiation from the low iota target is reflected by the vertical target. The baffle plates surrounding the target are blocking the camera view at the bottom. The high iota target is furthest from the camera, leading to blocking as a result of low resolution.

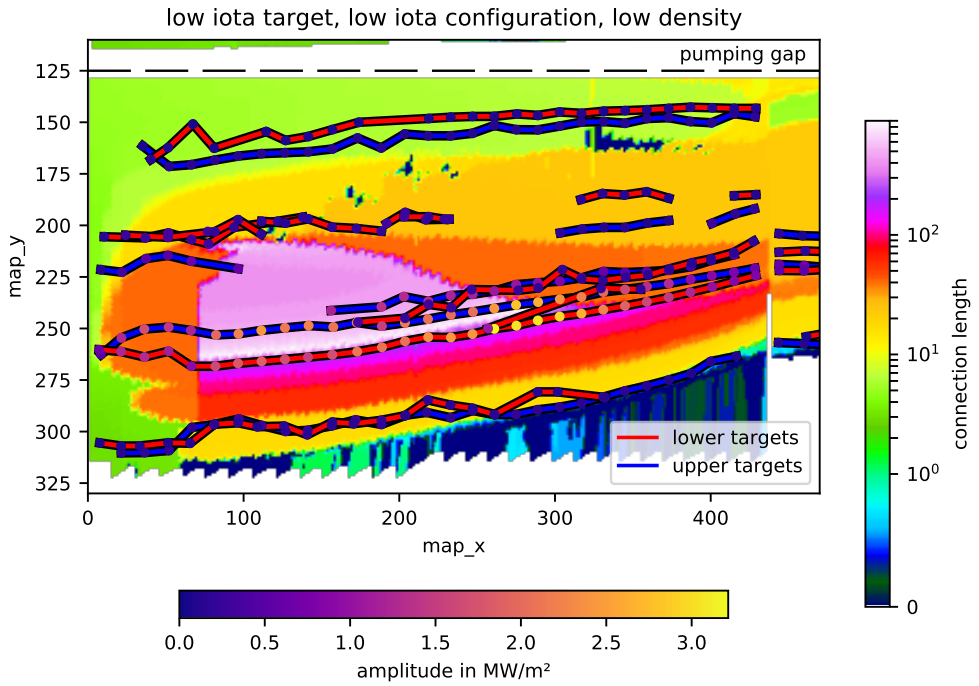


**Figure 26:** The features on the low iota target from discharge #20180829.009 in the low iota configuration are overlaid on top of a map of the connection lengths. The connection lengths where calculated without taking error fields or toroidal current into account. From the toroidal current, one would expect the map to be shifted slightly up for the lower targets and down for the upper targets. The feature at the bottom is an artifact resulting from the baffle plates next to the target plates, which are blocking the view of the camera. From the connection lengths, the different topological regions can be differentiated. The island SOL (purple/pink) in the center with long connection lengths is bordered by the TSR(orange) (UTS for upper, LTS for lower targets) on the left and right. Below is the private flux region PF (red).

## 6.2 Strike Line Movement

The movement of the strike lines is expected to be toroidally homogeneous [3]. This is not really the case here. The accuracy of the movement speed depends on how accurate the position of the Gaussian can be determined. For wider Gaussian's, the accuracy to which the Gaussian's position can be determined is reduced. Increasing density leads to a wider strike line, so for higher densities the variation of the movement speed increases. In general, a trend in the expected direction can be seen for the main strike line. In the standard configuration the island size is decreased by the poloidal magnetic field generated by the tororoidal current [29]. In low iota configuration the island size increases. The fitting accuracy of any other features was however not sufficient for analysis. For a single finger with good fit quality like in fig. 14b, the movement of the strike line over time compared to stationary features can be seen, an even better example at higher density is provided in fig. 16. Here the moving strike line between the upper and lower deposits is clearly visible.

### 6.3 Scrape-off Layer Transport

In this section an attempt is made to make a connection between some of the transport mechanisms introduced in section 3.5 and the strike line parameters observed in section 3.6.

The poloidal $\mathbf{E} \times \mathbf{B}$ drift, contributing to perpendicular transport, increases the transport along the LCFS into the direction of the lower target shadow region LTS, illustrated in fig. 27. At the same time heat-flux from inside the PFR enters the UTS. This means that on upper and lower targets heat-flux arrives from different sources into the TSR. This effect can be seen in the low-iota low density case fig. 18. The strike line in the TSR from $\Phi \approx -18°$ to $-15.5°$ has a considerably greater width on the lower targets, which receive heat-flux from the LTS, than on the upper targets, which receive their heat-flux from the UTS. Because of the short connection lengths, not much perpendicular transport takes place in the PFR, leading to a narrow strike line. As expected from the density dependency of perpendicular heat-flux $q_\perp \propto n$, the strike line width increases with the density. In all discharges, excluding the phenomenon in the TSR discussed above, the strike line width slightly decreases toroidally in the SOL region for both low density cases shown in fig. 18, 21. It stays constant for the higher density discharges. This toroidal distribution can also be seen in the toroidal distribution of the power [4].

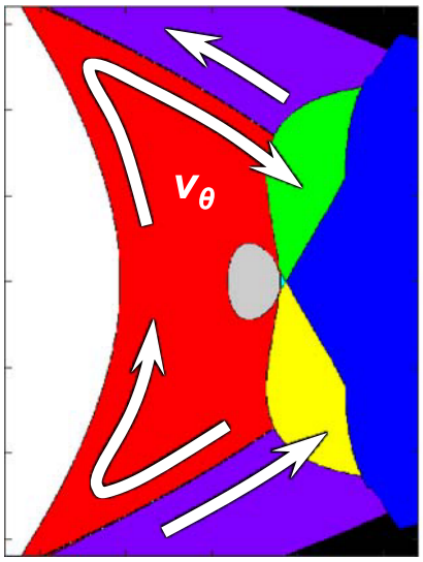


**Figure 27:** Illustration of poloidal drift flow ($\nu_\Theta$) patterns in the island SOL (red) and PFR (purple) for the low iota configuration. Reproduced from [18]. The LTS (green) and UTS (yellow) receive different amounts of heat-flux from island SOL und PFR.

# 7 Conclusion

A tool to parameterise the target heat-flux data has been developed and used to analyse the heat-flux of several experiments. The challenges with target surface deposits and their influence are discussed. Surface deposits explain why multiple features are predominantly present at higher densities. Two density scans in low-iota and standard magnetic configuration have been analysed and the influence of transport on strike line parameters is discussed. A number of improvements to the routine can be made. In [4] it was assumed that the strike line consists of a broad and a narrow feature. The here presented analysis suggests that this broad feature is in fact the main strike line with the overestimated heat-flux of the deposits next to it. This should be taken into account, for example by fitting these features individually and not as a broad underlying Gaussian. Further improvements to the fitting routine can be made by determining the position of deposits from the analysis done here and removing those data points, since the heat-flux profile produced by the deposits can not always be approximated by Gaussians. Because of short connection lengths, the strike line in the TSR does not have a Gaussian shape but an exponentially decaying profile. An addition to the code should be made to fit these regions with equation 24 or 25.

# 8 Appendix

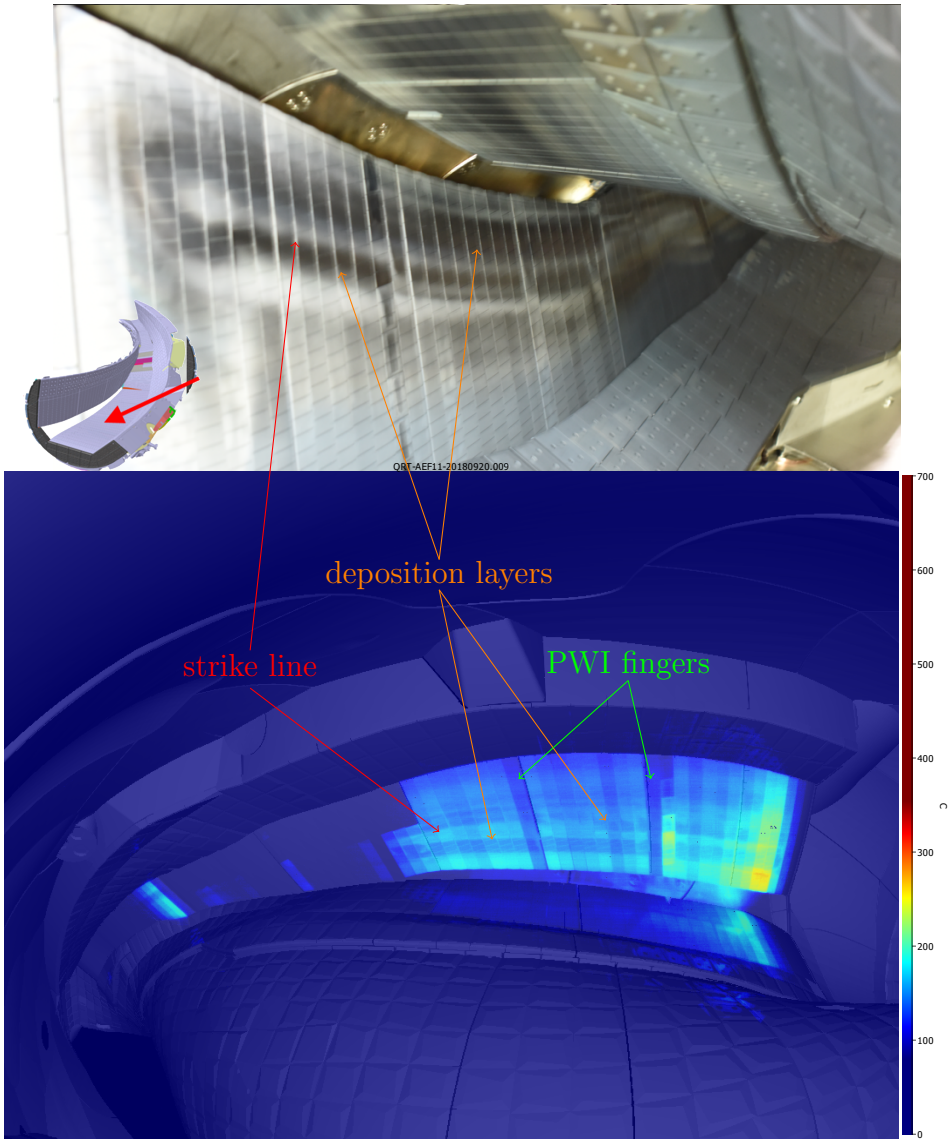


**Figure 28:** bottom: The Surface temperature of experiment #20180920.009 before plasma loading, as seen by the infrared camera. The deposits left and right to the region where the strike line hits are being insulated by the deposits. They emit less thermal radiation than the rest of the target when not loaded with plasma, which has been heated up from previous experiments. Marked is the strike line for the standard configuration. Also shown are the PWI fingers, which have different thermal properties and have to be excluded from the analysis. top: Shown is a photo taken of a target after OP 1.2. The white regions where the tiles have been eroded by the plasma and the darker deposits are clearly visible. The images have kindly been provided by Dr. Marcin Jakubowski.

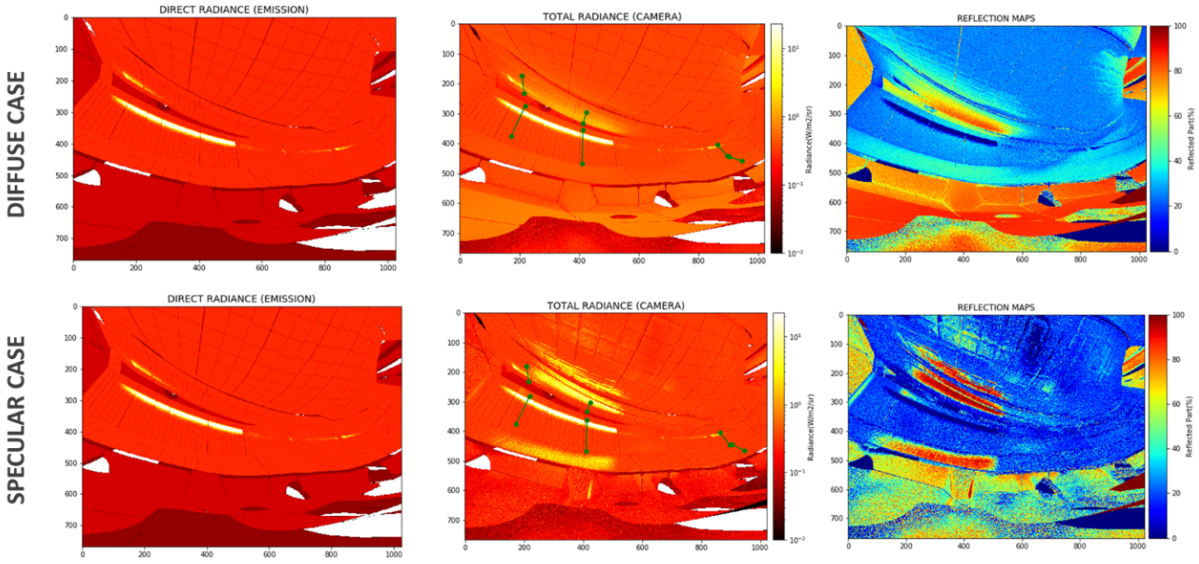


Figure 4: Synthetic images in radiance for standard scenario for diffuse and specular case (Left): reflection-free images (Middle): Total collected flux (Right): Reflection maps giving the reflected flux part over total collected flux

**Figure 29:** Ray-tracing analysis of radiance for the standard configuration. A significant amount of radiation from the main strike line is reflected by the vertical target.

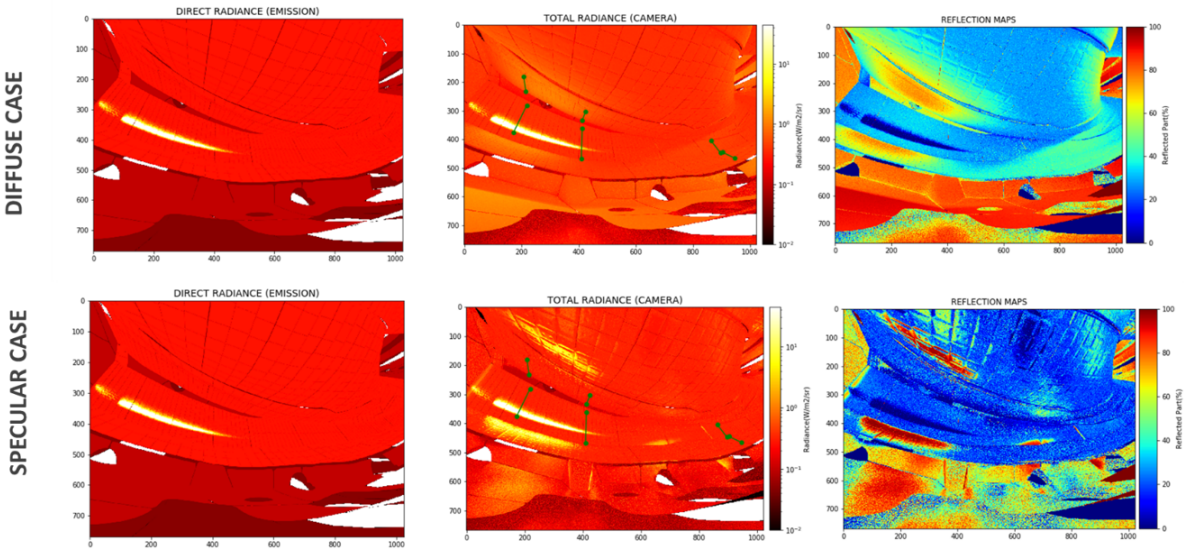


Figure 18: Synthetic images in radiance for low iota scenario for diffuse and specular case. (Left): reflection-free images (Middle): Total collected flux (Right): Reflection maps giving the reflected flux part over total collected flux

**Figure 30:** Ray-tracing analysis of radiance for the low-iota configuration. No significant amount of radiation is reflected onto the targets, only the baffle plates reflect some radiation.

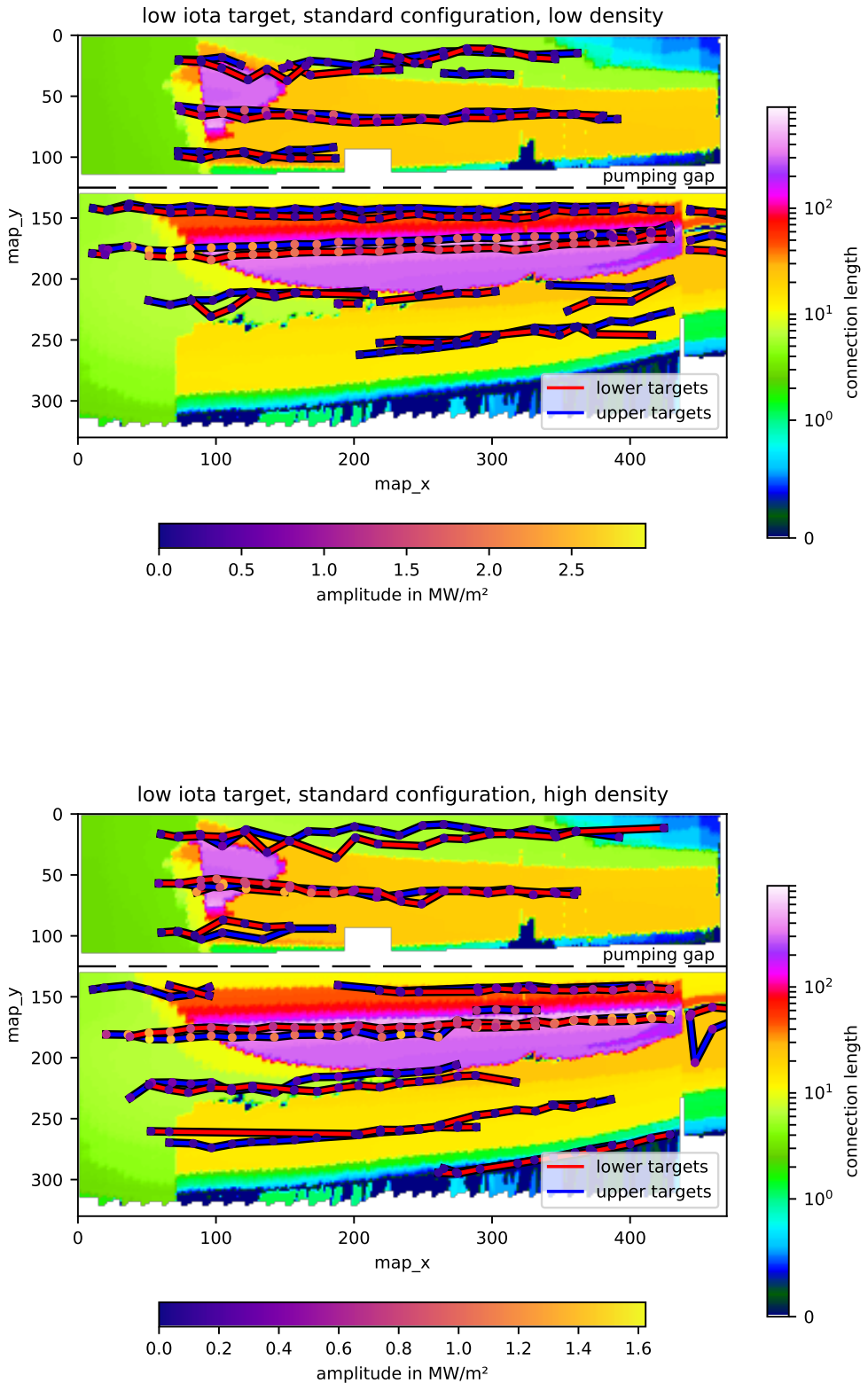


**Figure 31:** Standard configuration discharges #20180920.017 and #20180829.026 overlaid on top of a map of the connection lengths of the field lines intercepted by the target. The deposits next to the strike line are at the same positions as in the low iota configuration figs. 26, 32. On the vertical target the reflections are at map_x $\approx 25$ above the strike line.

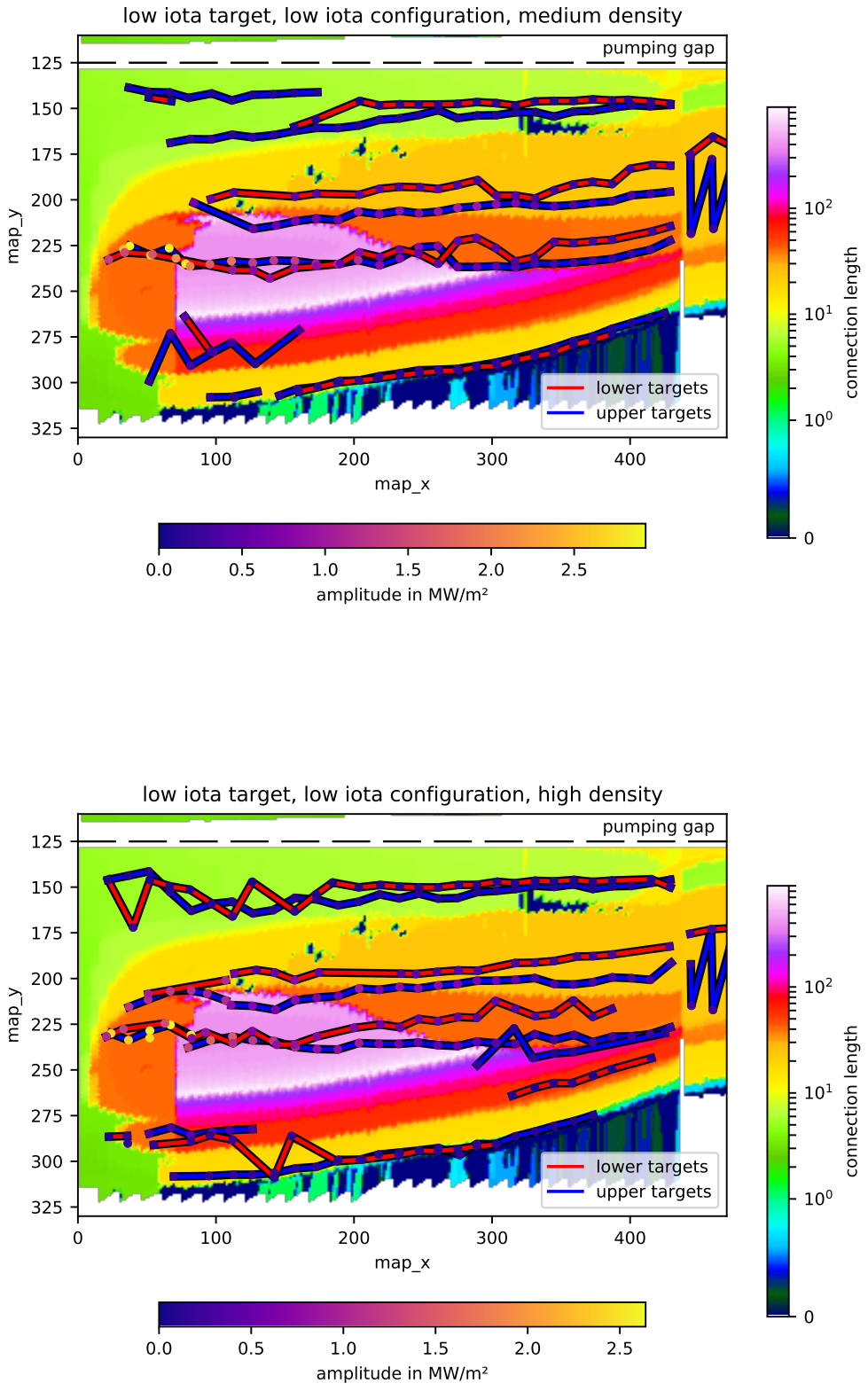


**Figure 32:** Low iota discharges #20180829.017 and #20180829.026 overlaid on top of a map of the connection lengths of the field lines intercepted by the target. See fig. 26 for more detail. The deposits at map_x $\approx$ 150 and map_x $\approx$ 200 are more pronounced here. The strike line seems to shift closer to the pumping gap compared to the low density case fig. 26.

# References


[1]B. Sieglin, "Experimental Investigation of Heat Transport and Divertor Loads of Fusion Plasma in All Metal ASDEX Upgrade and JET", PhD thesis (TU München, 2014).

[2]F. F. Chen, "Introduction to plasmaphysics and controlled fusion", in (Springer, 2018).

[3]Y. Gao, M. W. Jakubowski, P. Drewelow, F. Pisano, A. Puig Sitjes, H. Niemann, A. Ali, and B. Cannas, "Methods for quantitative study of divertor heat loads on W7-X", Nuclear Fusion **59**, 10.1088/1741-4326/ab0f49 (2019).

[4]D. Bold, F. Reimold, H. Niemann, Y. Gao, M. Jakubowski, C. Killer, and V. R. Winters, "Parametrisation of target heat flux distribution and study of transport parameters for boundary modelling in W7-X", Nuclear Fusion **62**, 1–15 (2022).

[5]M. Jakobs, N. Organisatie, and W. Onderzoek, "Fusion Energy-Burning Questions", PhD thesis (2016).

[6]J. Wesson, "Tokamaks", in (Oxford University Press, 2011).

[7]MPI für Plasmaphysik, *Concept planning*, [Online; accessed 02-01-2024].

[8]J. Lyman Spitzer, "The stellarator concept", Phys. Fluids **1** (1958).

[9]C. Mercier, "Equilibrium and stability of a toroidal magnetohydrodynamic system in the neighbourhood of a magnetic axis", Nuclear Fusion **4**, 213–226 (1964).

[10]P. Helander, C. D. Beidler, T. M. Bird, M. Drevlak, Y. Feng, R. Hatzky, F. Jenko, R. Kleiber, J. H. Proll, Y. Turkin, and P. Xanthopoulos, "Stellarator and tokamak plasmas: a comparison", Plasma Physics and Controlled Fusion **54**, 10.1088/0741-3335/54/12/124009 (2012).

[11]F. Giorgetti, "An integrated multi-physics tool for the mechanical analysis of fusion reactors superconducting magnets", 10.13140/RG.2.2.15543.78247 (2019).

[12]F. Wagner, "Physics of magnetic confinement fusion", 10.1051/C (2013).

[13]C. Killer, Y. Narbutt, and O. Grulke, "Turbulent transport in the scrape-off layer of Wendelstein 7-X", Nuclear Fusion **61**, 10.1088/1741-4326/ac1ae3 (2021).

[14]E. Strumberger, "Sol studies for W7-X based on the island divertor concept", Nuclear Fusion **36**, 891–908 (1996).

[15]R. König, P. Grigull, K. McCormick, Y. Feng, J. Kisslinger, A. Komori, S. Masuzaki, K. Matsuoka, T. Obiki, N. Ohyabu, H. Renner, F. Sardei, F. Wagner, and A. Werner, "The divertor program in stellarators", Plasma Physics and Controlled Fusion **44**, 2365–2422 (2002).

[16]S. A. Lazerson, Y. Gao, K. Hammond, C. Killer, G. Schlisio, M. Otte, C. Biedermann, M. Spolaore, S. Bozhenkov, J. Geiger, O. Grulke, D. Nicolai, G. Satheeswaran, H. Niemann, M. Jakubowski, P. Drewelow, A. P. Sitjes, A. Ali, B. Cannas, F. Pisano, R. König, G. Wurden, G. Kocsis, T. Szepesi, U. Wenzel, M. Mulsow, K. Rahbarnia, J. Schilling, U. Neuner, T. Andreeva, H. Thomsen, J. Knauer, K. J. Brunner, B. Blackwell, M. Endler, S. Klose, and L. Rudischhauser, "Tuning of the rotational transform in Wendelstein 7-X", Nuclear Fusion **59**, 1–23 (2019).

[17]H. Renner, D. Sharma, J. Kißlinger, J. Boscary, H. Grote, and R. Schneider, "Physical aspects and design of the wendelstein 7-X divertor", Fusion Science and Technology **46**, 318–326 (2004).

[18]K. C. Hammond et al., Plasma Phys. Control. Fusion **61** (2019).

[19]D. M. Kriete, A. Pandey, V. Perseo, J. C. Schmitt, D. A. Ennis, D. Gradic, K. C. Hammond, M. Jakubowski, C. Killer, R. König, D. A. Maurer, F. Reimold, V. Winters, M. N. Beurskens, S. A. Bozhenkov, K. J. Brunner, G. Fuchert, J. Knauer, E. Pasch, and E. R. Scott, "Effects of drifts on scrape-off layer transport in W7-X", Nuclear Fusion **63**, 10.1088/1741-4326/acab75 (2023).

[20]P. C. Stangeby, "The Plasma Boundary of Magnetic Fusion Devices", The Plasma Boundary of Magnetic Fusion Devices, 10.1887/0750305592 (2000).

[21]Ralf Schneider. private communication. Institute of Physics, University of Greifswald.

[22]"Measurements of plasma parameters in the divertor island of Wendelstein 7-X through line-ratio spectroscopy on helium", Nuclear Fusion **60**, 10.1088/1741-4326/aba9eb (2020).

[23]P. C. Stangeby and A. V. Chankin, "Simple models for the radial and poloidal E × B drifts in the scrape-off layer of a divertor tokamak: Effects on in/out asymmetries", Nuclear Fusion **36**, 839–852 (1996).

[24]O. E. Garcia, R. A. Pitts, J. Horacek, A. H. Nielsen, W. Fundamenski, J. P. Graves, V. Naulin, and J. J. Rasmussen, "Turbulent transport in the TCV SOL", Journal of Nuclear Materials **363-365**, 575–580 (2007).

[25]M. Endler, "Turbulent SOL transport in stellarators and tokamaks", Journal of Nuclear Materials **266**, 84–90 (1999).

[26]C. Killer, B. Shanahan, O. Grulke, M. Endler, K. Hammond, L. Rudischhauser, and W.-X. Team, "Plasma filaments in the scrape-off layer of Wendelstein 7-X", Plasma Physics and Controlled Fusion **62**, 85003 (2020).

[27]A. Herrmann, W. Junker, K. Gunther, S. Bosch, M. Kaufmann, J. Neuhauser, G. Pautasso, T. Richter, and R. Schneider, "Energy flux to the ASDEX-Upgrade diverter plates determined by thermography and calorimetry", Plasma Physics and Controlled Fusion **37**, 17–29 (1995).

[28]Pedregosa et al., "Scikit-learn: machine learning in python", Journal of Machine Learning Research, 2825–2830 (2011).

[29]J. Geiger, C. D. Beidler, M. Drevlak, H. Maaßberg, C. Nhrenberg, Y. Suzuki, and Y. Turkin, "Effects of net currents on the magnetic configuration of W7-X", Contributions to Plasma Physics **50**, 770–774 (2010).

# Acknowledgments

I would like to express my gratitude to Prof. Dr. Ralf Schneider for letting me chose this interesting research topic. Additionally, I would like to thank Prof. Dr. Thomas Klinger for agreeing to be my second examiner. I'm extremely grateful to Dr. David Bold and Dr. Felix Reimold for giving me the opportunity to work on this topic at IPP, as well as for their guidance and helpful feedback throughout the whole thesis. I would also like to thank Dr. Yu Gao and Dr. Marcin Jakubowski for their help with the infrared diagnostic as well as Amit Kharwandikar for his help with SMoLID.